The influence of sediment blanketing on subduction-zone seismicity

Dan M^{c}Kenzie[1] James Jackson
Bullard Laboratories of the Department of Earth Sciences
Madingley Road
Cambridge CB3 0EZ U.K.
August 18, 2020

Abstract

Subduction of oceanic lithosphere is now occurring beneath the Aegean and central Caspian Seas, and beneath the Indo-Burman Ranges in NE India, generating zones of earthquakes that reach depths of more than 150 km. Their existence is surprising. In general, where the temperature of the mantle part of the oceanic lithosphere can be estimated, earthquakes are confined to material whose temperature is below 600°C. In these three regions the oceanic lithosphere is overlain by sediments with low thermal conductivity whose thickness is probably 10-25 km. The temperature of the oceanic crust and upper half of the lithosphere should be considerably increased by such a thick sedimentary cover, yet there is no obvious difference between these subduction zones and those where there is little sediment on the subducting plate. Detailed thermal modeling of the temperature shows that, for the first 40 Ma, the deposition of even a thick sedimentary layer has little effect on the thickness of the region of lithosphere whose temperature is below 600°C. The modest effect of sediment blanketing over a period as long as 40 Ma was quite unexpected. Over the next 200 Ma the lithospheric temperature increases, until the Moho temperature reaches $\sim$ 600°C. This behaviour has important implications for oil and gas generation in the sediments, and for the existence of large earthquakes at depths of 150 km or more beneath the Hindu Kush, Pamirs and Romania.

1. Introduction

Margins of continents often consist of sediment accumulations whose thickness can be 15-20 km or more. The sediments consist of material that has been eroded from continents and deposited on oceanic crust, or on continental crust that has been strongly stretched. If the volumes of sediment are large they are likely to have been transported by major river systems and deposited in deltas. However, because the thin crust is commonly overlain by thick sediments, it is generally difficult to determine whether it was originally oceanic or continental. In some places, where the initial spreading rate was less than 10 mm/a, upwelling may have been too slow to cause the mantle to melt, and it is difficult to determine if any crust even existed before the sediments were deposited. The sea floor adjacent to rifted margins is generally the oldest part of any ocean, and is the last part to be subducted when continents collide. Unlike rifted margins, the margins of converging continents have different shapes. Therefore small pieces of oceanic lithosphere will remain during the initial stages of continental collision. The western and eastern Mediterranean, the Black and the Caspian Seas are all remnants formed in this way, when the continents to the south collided with Eurasia. Except for the western Mediterranean, most of whose sea floor has been produced by back-arc spreading in the last 30 Ma, the age of that underlying the eastern Mediterranean and the Caspian Sea is not well determined, though it is probably at least Cretaceous ($\sim$100 Ma). Though the original oceanic lithosphere is now buried beneath more than 10 km of sediment, it still produces seismically active slabs where it is being subducted beneath the Aegean Arc and the Apscheron Sill in the Caspian Sea (Fig. 1), with earthquake depths of more than 100 km. The subduction of old lithosphere in the western Mediterranean generated slabs that are still seismically active, though subduction has now stopped.

[1]Corresponding author. E-mail: mckenzie@madingley.org

The controversial question with which this paper is principally concerned is whether seismically active slabs beneath the Hindu Kush, the Pamirs and Vrancea in Romania result from the subduction of oceanic lithosphere, as McKenzie et al. (2019) have argued, or of continental lithosphere, as many others (Kufner et al. 2016, 2017, Lorinczi & Houseman 2009, Molnar & Bendick 2019, Schneider et al. 2013, Sippl et al. 2013a,b) believe. McKenzie et al.'s argument depends on the relationship between seismicity and temperature. McKenzie et al. (2005, 2019) carried out detailed global studies of earthquake depths at locations where the temperature could be estimated, beneath oceans, continents and within subducted slabs. They showed that only those regions of the crust and mantle whose temperature is less than 600°C are seismically active. Most of the continental lithosphere beneath the Moho is hotter than 600°C, and no earthquakes approaching the size of the magnitude 7.5 earthquakes that occur beneath the Hindu Kush are known from the mantle beneath the continents, whereas earthquakes of this magnitude occur in the mantle beneath the oceanic Moho and in slabs of subducted oceanic lithosphere. McKenzie et al. (2019) used this simple observation to argue that the sinking slabs beneath the Hindu Kush, the Pamirs and Vrancea in Romania also result from the subduction of oceanic crust and lithosphere, though there is no obvious geological evidence at the surface that such subduction has occurred. GPS measurements and the absence of earthquakes show that no shortening is now taking place beneath Vrancea, the Pamirs or the Hindu Kush (N. D'Agostino, personal communication, Perry et al. 2019). Furthermore the regional crustal structure beneath the Pamirs suggests that Indian crust and lithosphere is now in contact with Asian crust and lithosphere (Mechie et al. 2012), with no intervening buried oceanic lithosphere. If McKenzie et al. are correct, some of the adjacent regions that are now above sea level are likely also be underlain by oceanic lithosphere which has been covered by a large thickness of sediment.

Major pre-existing river systems that drain approaching continents will be diverted from the places where the continents first come in contact by the formation of fold mountain belts. The rivers will instead feed their sediment into the small ocean basins formed by the irregular boundaries of approaching continents. Examples of such rivers are the Rhone and the Nile, feeding into the Mediterranean, the Danube and the Don feeding into the Black Sea, and the Volga and the Amu Darya (before it moved to the Aral Sea) into the Caspian. The Ganges and the Brahmaputra have deposited the largest such accumulation (Curray 1994, Acton et al. 2010, Mitra et al. 2018) on Early Cretaceous (120-135 Ma, Davies et al. 2016) oceanic lithosphere in the NE Indian Ocean. Oceanic crust of the same age probably also underlies the region of eastern India and western Myanmar, shown in Fig. 2, where the Indo-Burman Range is underlain by eastward-dipping thrusts which are overriding Eocene ($\sim$ 40 Ma) sediments whose thickness is greatest in the NE (Acton et al. 2010, Kumar et al. 2015). Subduction beneath the Range has generated volcanism and a seismically active slab that dips to the east. The earthquakes further south and west, beneath the Bay of Bengal (Fig. 2), extend from depths of 30 km to 50 km beneath thick sediments deposited on oceanic crust (Mitra et al. 2011). In this region no earthquakes whose depth can be accurately determined occur at depths shallower than 30 km (see supplementary material).

Deposition of sediment in small ocean basins will continue until they are filled to sea level. The depth of sediment-free ocean formed in the Jurassic or Cretaceous, with a crustal thickness of 7 km, is now about 6 km, and is sufficiently old to have reached a thermal steady state. If the sea water is replaced by sediment with a density of 2.75×10^3 kg m^{-3} and the basin is isostatically compensated, the thickness of sediment required to fill the basin to sea level is about 25 km. In Romania the age of the sediments in contact with the basement to the SE of Vrancea is unknown. In contrast, large thicknesses of sediment are unlikely to have been deposited in eastern India, Bangladesh and western Myanmar until India collided with Eurasia about 40 Ma ago.

This outline shows that McKenzie et al.'s argument depends on the empirical observation, that the cut-off temperature for earthquakes everywhere in the mantle is about 600°C, and not in any way

on the controversial issue (see, for instance, Frohlich 2006) of the physical mechanism that produces earthquakes in sinking slabs. McKenzie et al.'s proposal requires a substantial thickness, of perhaps 30 km, of lithosphere to remain at a temperature below 600°C for as long as ~ 40 Ma beneath ~ 25 km of sediment. They did not examine this issue, which is the main concern of this paper. The next two sections are concerned with modelling the thermal evolution of the crust and lithosphere during and after a period of rapid sedimentation, and the last section discusses the implications of the resulting thermal models. As the discussion below shows, the thermal evolution of the oceanic lithosphere buried in this way depends on the poorly-known values of a number of different parameters. The most seismically active slabs beneath continental crust are those beneath the Hindu Kush, the Pamirs and the Indo-Burman ranges. These slabs are likely to be associated in some way with the oceanic subduction and continental shortening as India moved northwards. Knowledge of the kinematics of this collision is therefore used as a framework for the modelling, to reduce the number and range of the parameters that need to be varied in the numerical experiments. The experiments show that the thermal behaviour is relatively simple, and that they can be used to predict the behaviour of the oceanic lithosphere under a wide variety of different conditions.

2. Governing equations

The problem outlined in the introduction, of the time-dependent thermal behaviour of the oceanic crust and lithosphere when a thick layer of cold sediments is deposited on top, is not difficult to solve. However, it is important to model the temperature of both the crust and the lithosphere, and not simply the crust with a fixed basal heat flux, because the temperature of the lithosphere and the heat flux through the Moho are strongly time dependent. Carslaw & Jaegar (1959, p388 eq.7) give an analytic solution which assumes that the sedimentation rate is constant, there is no heat generation by radioactive decay and that thermal conductivity is everywhere the same and is independent of temperature. Their solution is easily programmed, and shows that the temperature of the lithosphere is little affected by the addition of cold material to the surface. It therefore seemed worthwhile to make the thermal model more flexible and realistic, using a similar numerical scheme and conductivity to that of McKenzie et al. (2005). This scheme takes account of radioactive heat generation in the sediments, the difference in thermal conductivity between crust and mantle, and the temperature dependence of the thermal conductivity. The modelling was divided into two steps. The first calculated the thermal evolution of oceanic lithosphere as it was blanketed by sediments. The second used the resulting geotherm of oceanic crust and lithosphere as the initial condition for the subducting slab. The temperatures from the two steps are shown in separate panels in the figures.

The equation governing the temperature in the sediments is most easily solved in a frame fixed to the surface of the sediments, whose temperature is fixed to 0°C in all the experiments described below. In this frame the sediments, the oceanic crust and lithosphere move downwards, and the resulting advection of heat must be taken into account. This approach is known as an Eulerian specification. However, the thermal history of the oceanic lithosphere is easier to understand in a frame that is fixed to the Moho, called a Lagrangian specification. In this frame the surface of the sediments moves upwards. However, applying the boundary condition at the sediment surface in a moving frame is difficult, so it is convenient to solve the problem using an Eulerian scheme, and then transform the solution into a frame fixed to the Moho using a Gallilean transformation

$$z = z_l - ut \tag{1}$$

where z is the depth below the surface of the sediment, z_l that below the top of the oceanic crust, and u the sedimentation rate, which is taken to be constant or 0 in the experiments described below.

The Lagrangian specification of the equation governing the conservation of energy during the first step is

$$\frac{D}{Dt}(\rho C_p T) = \frac{\partial}{\partial z}\left(k\frac{\partial T}{\partial z}\right) + H \tag{2}$$

where ρ is the density and C_p the specific heat of the material, T is the temperature in °C, k the thermal conductivity and H the rate of heat generation.

The thermal conductivity results from two processes; heat transport by lattice conductivity involving phonons, and by radiative transfer by photons. The first contribution is now generally determined by measuring the thermal diffusivity $\kappa_l = k_l/\rho C_p$, whereas that from radiative transfer k_r is calculated from the optical properties of the material, and is only important at high temperatures. Rewriting equation (2) in Eulerian form and neglecting the variation of ρ and C_p with temperature (McKenzie et al. 2005) gives

$$\frac{\partial T}{\partial t} = \frac{\partial}{\partial z}\left(\kappa\frac{\partial T}{\partial z}\right) - u\frac{\partial T}{\partial z} + \frac{H}{\rho C_p} \tag{3}$$

where the diffusivity κ is given by

$$\kappa = \kappa_l + k_r/(\rho C_p)$$

The second step involves calculating the thermal evolution of a sinking slab with the initial temperature distribution given by the first step, and with the upper and lower temperatures of the slab fixed to the mantle potential temperature. The figures show the resulting steady state solution. Unlike the first step, conductive heat transport occurs both along, $\kappa\,(\partial T/\partial x)$, and normal, $\kappa\,(\partial T/\partial z)$, to the sinking lithosphere. McKenzie (1969) showed that $va/\kappa \gg \pi$ for most subduction zones, when $\partial T/\partial z \gg \partial T/\partial x$. If the thermal conductivity is constant McKenzie's analytic solutions can be used to calculate the down-dip distance to which the 600°C isotherm extends when $\partial T/\partial x$ is ignored, 1D conduction, and when it is included, 2D conduction. When the subduction velocity v is 10 mm/a, the smallest value used in the numerical experiments, the distances are 67.3 km (1D) and 67.8 km (2D). The difference between the two values becomes smaller as the velocity increases. Conductive heat transport along the slab was therefore ignored. Heat generation within the oceanic crust and lithosphere are both small (see below) and can also be ignored. Then equation (2) can be written as

$$v\frac{\partial T}{\partial x} = \frac{\partial}{\partial z}\left(\kappa\frac{\partial T}{\partial z}\right) \tag{4}$$

or, using the Lagrangian specification

$$\frac{\partial T}{\partial t} = \frac{\partial}{\partial z}\left(\kappa\frac{\partial T}{\partial z}\right) \tag{5}$$

Equation (5) shows $T = T(t, z)$ and is independent of v. Therefore any solution to equation (5) that satisfies the boundary conditions at $x = 0$ does so for all values of v. Many of the contour plots illustrated below use a subduction velocity of 50 mm/a. Equation (5) shows that solutions corresponding to other subduction velocities can be obtained simply by an appropriate change in the down-dip length scale.

Equation (5) was solved using the same numerical scheme as McKenzie et al. (2005) used (Press et al. 2007, pp 1047-8), which is unconditionally stable. For accuracy the time step Δt was taken to be the smaller of

$$\frac{\Delta z^2}{2\kappa} \quad \text{and} \quad \frac{\Delta z}{v}$$

where $\Delta z (= a/200)$ is the depth step. The step change in thermal conductivity at the base of the oceanic crust required the finite difference equation for the point centred on the Moho to be written in conservative form (see supplementary material).

Two effects have not been included in the simple model used below. The first is dissipative heating. Friction on the fault that produces the sinking slab will generate heat. However, the hanging wall of this fault is cooled from both above and below. Therefore such heating will have little effect on the temperature. Viscous heating in the wedge above the slab is also unlikely to be important, because its viscosity is lowered by the release of water from the slab.

Another effect that is ignored is the presence of a cool thermal boundary in the wedge above the sinking slab, which must be generated by heat loss to the slab (Davies 1999, Emmerson & M^{c}Kenzie 2007, van Keken et al. 2008). The temperature gradient in this boundary layer depends on the flow field within the wedge, which in turn is controlled by viscosity variations (van Keken et al. 2008). However, the presence of such a boundary layer can only decrease the rate at which the slab gains heat from the overlying wedge, and therefore must increase the depth to which the 600°C isotherm descends. Therefore the simple model used below provides a lower bound on this depth, which can only be increased by more elaborate calculations.

3. Parameter values

Equations (3) and (5) require the values of a number of parameters to be specified. Wherever possible the values chosen were based on laboratory measurements, which were not modified to improve the agreement between the models and the geophysical observables. But the values of some important parameters, such as the thickness of the oceanic lithosphere, its base and initial potential temperature, which cannot be directly measured, were based on models that in turn depend on laboratory measurements. Initial experiments showed that the thermal evolution was especially sensitive to the age of the lithosphere when sedimentation starts and to the thermal conductivity of the sediments. The best available estimates were used to construct a reference model. Numerical experiments were then carried out to discover the sensitivity of the thermal evolution to various parameters, which were either the ones that were poorly known or those that are likely to be variable.

If the temperature dependence of ρC_p and κ in equation (3) are ignored, the temperature in the first step is controlled by the dimensionless parameters $Ha^2/(k_s T_p)$ and ua/κ and the second by va/κ alone (see supplementary material). The value of H is by far the most variable. In the convecting upper mantle its value is about $1.2 \times 10^{-3} \mu$W m^{-3}, contrasting with a value of $2 \times 10^{-2} \mu$W m^{-3} in the oceanic crust and 1.65 μW m^{-3} in the upper part of the continental crust (Rudnick & Gao 2005, Jaupart & Mareschal 2005). Heat generation in oceanic crust and mantle was therefore ignored in all the numerical experiments described below, and that of the sediments taken to be that of the upper crust, of 1.65 μW m^{-3}. The value of ua/κ is principally controlled by that of u, the sedimentation velocity. The water depth above old oceanic lithosphere is about 6 km. If the water is replaced by 25 km of isostatically compensated sediment, giving a crustal thickness of 32 km, the average density of the sediment is 2.75×10^3 kg m^{-3}. The temperature variation within the oceanic crust and lithosphere depends on the sedimentation history, as well as the total thickness of sediments deposited.

The density, specific heat, and thermal diffusivity of the crust and mantle, and their variation with temperature, were calculated from Grose & Afonso's (2013) expression for the phonon contribution to thermal diffusivity

$$\kappa = a + b \exp(-T/c) + d \exp(-T/e) \tag{6}$$

(corrected here for a misprint in Grose & Afonso (2013), Grose, personal communication).

The contribution that radiation makes to the thermal conductivity of olivine, k_r, is controversial (Hofmeister 2014, Grose & Afonso 2019). It depends on the opacity and the (unknown) grain size in the mantle. If Hofmeister's expressions are correct, the increase in diffusivity resulting from radiation is unimportant. In contrast, if the grain size is greater than about 0.1 mm Grose & Afonso's expressions produce a value of k_r that has an influence on the temperature in the lower half of the oceanic lithosphere. Because of this disagreement, and because no direct measurements of the radiative contribution to the conductivity have yet been carried out, it was ignored.

The potential temperature T_p of the upwelling mantle controls the thickness of the oceanic crust, the initial temperature of the oceanic lithosphere, and the temperature within the subducting slab. White et al. (1992) estimated the average thickness of the oceanic crust to be 7.1 ± 0.8 km. A more recent estimate by Christeson et al. (2019) is 6.15 ± 0.93 km. A value of potential temperature of 1300°C gives a crustal thickness of 5.8 km using Katz et al.'s (2003) parameterisation of the melt fraction as a function of depth, an entropy of 400 J kg^{-1} °C^{-1} (Kojitani & Akaogi 1997), and a water content of the source of 0.01%, increasing to 7.7 km for a potential temperature of 1325°. The uncertainty in value of T_p is therefore unimportant, and a value of 1312°C, giving a crustal thickness of 6.65 km, was used in the numerical experiments.

Grose & Afonso's (2013) model of thermal diffusivity, combined with a mantle potential temperature of 1312°C and a plate thickness of 100 km, results in a thermal model for the cooling of an oceanic plate that agrees with the variation of heat flow (Hasterok 2013) and water depth (Crosby et al. 2006, Hoggard et al. 2017) with age. The greatest depth of intraplate oceanic earthquakes (Craig et al. 2014), determined by modelling their waveforms, is less than that of the 650°C isotherm, and is within one standard deviation, of 3 km, of the 600°C isotherm. Re-determination of the depths of two earthquakes (Chinn & Isacks 1983, Andrews et al. 2020) which were reported to be at depths where the temperature is greater than 600°C, shows that they occurred at shallower depths where the temperature is less than 600°C (Craig et al. 2014, Supplementary Material). The thermal model of the oceanic lithosphere used below is therefore both well constrained and compatible with the relevant observations.

The thermal diffusivity of the igneous crust and sediments is complicated by the large difference between that of quartz, of about 7×10^{-6} m^2 s^{-1} (Branlund & Hofmeister 2007), anorthite-rich feldspar (Branlund & Hofmeister 2012), of 0.7×10^{-6} m^2 s^{-1}, both at room temperature. Furthermore few laboratory measurements of the thermal conductivity of rocks specify their modal and mineral compositions in detail. The thermal conductivity of of the igneous crust at $T = 0$°C was taken to be 3.5 W m^{-1} °C^{-1} (Clark 1966, Clauser & Huenges 1995). A value for the thermal conductivity of sediments k_s, of 2.8 W m^{-1} °C^{-1}, was used for the reference model, which is within the range, of $2.6 - 2.8$ W m^{-1} °C^{-1}, that Bullard & Niblett (1951) determined for samples of Bunter Sandstone, an impure sandstone of Triassic age. These authors also give the thermal conductivity of Carboniferous shales, of $1.2 - 1.8$ W m^{-1} °C^{-1}, and of Millstone Grit, an impure quartzite with a thermal conductivity of $3.5 - 4.6$ W m^{-1} °C^{-1}. Bullard (1939) measured the thermal conductivity of samples of Witwatersrand Quartzite which contained between 75% and 90% quartz, of $6.3 - 8.0$ W m^{-1} °C^{-1}. The temperature dependence of the conductivity of crustal rocks is not an important source of uncertainty, because their temperature does not exceed 400°C in the models. Grose & Afonso's expression for the temperature dependence of k_s was therefore used to calculate the ratio of $k_s(T)/k_s(0)$ and the value of k_s scaled appropriately. In those experiments where 25 km of sediment was added to the oceanic lithosphere, the difference in the conductivity between the sediment and oceanic crust was ignored and the conductivity of the entire crust was taken to be that of the sediments.

4. Numerical experiments

The experiments were carried out in two steps. The thermal evolution of the system was started before subduction, using either the temperature of old oceanic lithosphere that had reached steady state, or that from one of a given age. A given thickness of sediment was then added over a specified period and the temperature evolution of the sediments, oceanic crust and lithosphere calculated using equation (3) with u set to the sedimentation rate. In the second step the resulting vertical temperature of the oceanic crust and lithosphere was used as the initial condition for the subduction. The results of the two steps are shown in the figures in two separate panels. Many of the experiments use a sedimentation history that starts 40 Ma ago, principally because rapid sedimentation on the margins of India is unlikely to have begun before India and Asia collided. Though the subduction rate v is taken to be 50 mm/a in many of the experiments, the behaviour for any other choice of v can be determined by scaling (see equation (5)).

The first two experiments, illustrated in Fig. 3, were designed to check that the numerical scheme gave correct estimates of the depth to which earthquakes extend within subduction zones whose oceanic lithosphere is covered by a thick layer of sediments before it is subducted. The subduction rate of the Hellenic Arc is about 40 mm/a, the age of the subducting lithosphere is probably greater than 100 Ma and the sediment thickness is $\sim$ 10 km (see Howell et al. 2017). The temperature of the oceanic crust and lithosphere was assumed to have reached steady state at the start of sedimentation, and the sediments to have been deposited at a constant rate over 120 Ma, followed by subduction. Fig. 3(a) shows that the 600°C isotherm extends about 400 km down-dip, or to a depth of about 255 km below the base of the lithosphere if the dip is 45°. This depth is somewhat greater than 150 km, the depth to which the seismicity extends, perhaps because the subduction has not yet been in progress long enough for the temperature to have reached steady state within the slab.

Fig. 3(b) shows a similar calculation for the Caspian, where the subduction velocity is $\sim$ 10 mm/a, the sediment thickness of 15 km is assumed to have been deposited at a constant rate over the last 20 Ma on an oceanic lithosphere whose temperature had reached a steady state. The 600°C isotherm extends about 120 km down-dip to a depth of 85 km, which is similar to the depth of the deepest earthquakes beneath the central Caspian Sea (see M^{c}Kenzie 2019).

Fig. 4(a) shows the thermal evolution of the model used as a reference for the other experiments. The initial temperature structure of the oceanic crust and lithosphere is that of the steady state. After the rapid sedimentation during the first 10 Ma, sedimentation stops. Over the next 40 Ma radioactive heat generation increases the temperature of the sediments, to more than 350°C at the contact between the sediment and the oceanic crust. However, because the upper 45 km of the oceanic lithosphere was cooler than 600°C when sedimentation started, a thickness of about 35 km is still below 600°C when subduction begins. The second panel shows that the subducted lithosphere remains seismogenic to a depth of almost 400 km.

The experiment illustrated in Fig. 4(b) is concerned with the influence of sedimentation history on the thermal structure. Instead of depositing the entire thickness of 25 km of sediment in the first 10 Ma, as is the case in the reference model at the top, the sediment is deposited at a constant rate throughout 50 Ma before subduction occurs. There is then less time for the temperature to be increased by radioactive heating than there is in the reference model, and more heat is lost by conduction to the surface through the thin layer of sediment during the early period after sedimentation begins. The seismogenic zone extends to a depth of 500 km.

The next pair of experiments illustrate the effect of the quartz content of the sediments. Fig. 5(a) shows the thermal evolution when the sediments are shale-rich, with a thermal conductivity at 0°C of 2.1 W m^{-1} °C^{-1}. Its low value allows more of the radioactive heat to be retained in the sediment, causing a greater increase in the temperature of the oceanic crust and upper mantle than takes place in the reference model. The resulting subduction zone is then only seismogenic to a depth of about 300 km. In contrast, when the sediments are quartz-rich (Fig. 5(b)) with a thermal conductivity

4.3 W m^{-1} $°C^{-1}$, more heat is lost by conduction to the surface, and the seismogenic zone extends to a depth of about 450 km.

The experiment illustrated in Fig. 6 shows the influence of the initial age of the oceanic lithosphere. Instead of using the steady-state temperature profile, the initial profile is that of 30 Ma old oceanic lithosphere. Though there is an initial thickness of oceanic crust and mantle of about 30 km that is cooler than 600°C when sedimentation starts, as sediment accumulates the temperature of this layer is increased by heat conducted from deeper in the lithosphere, and little remains sufficiently cool to be seismogenic when the lithosphere is subducted.

The last experiment, Fig. 7, shows the thermal evolution of the reference model when the oceanic crust and lithosphere remain at the surface for 250 Ma without undergoing subduction. After 200 Ma the temperature of the Moho reaches 600°C and seismicity is confined to the crust. The resulting thermal structure is typical of that of continental lithosphere.

5. Implications

The experiments described above have three important implications: for the origin of seismically active zones beneath continental interiors, for the formation of continental crust, and for the generation of oil and gas from organic-rich source rocks.

Figs. 4 and 5 show that old ocean lithosphere trapped within a continental collision zone and hidden beneath 25 km of sediment will remain seismogenic for at least 50 Ma. If it is then subducted, it can continue to generate earthquakes to a depth of more than 400 km. But this behaviour depends on the age of the underlying oceanic lithosphere on which the thick sediment is deposited. If the oceanic lithosphere is younger than about 30 Ma when sedimentation starts, Fig. 6 shows that its temperature will quickly rise above 600°C when it is subducted. If the seismically active zones beneath Vrancea, the Hindu Kush and the Indo-Burman Range are produced by subduction of the oceanic crust and lithosphere that lies beneath the thick layer of sediment, as M^{c}Kenzie et al. (2019) propose, the underlying lithosphere must have been sufficiently old ($\sim$ 60 Ma) to have cooled to close to its steady state temperature before sedimentation began.

Examples from the eastern Mediterranean and Caspian show that subduction may now be occurring with no visible signs at the surface, such as volcanoes or sutures (M^{c}Kenzie et al. 2019). A large horizontal thrust detachment may also exist within the crust, like that within the crust of Tibet (e.g. Craig et al. 2012), that causes the location of the surface shortening to be far removed from that at depth. In the case of the Hindu Kush and the Pamirs this argument requires there to have been a hidden basin, whose oceanic lithosphere was more than about 100 Ma old and only half the size of the Caspian Sea, to have been subducted in the last 15 Ma. We do not believe that the geological evidence can yet rule out this possibility. The nature of the thin crust beneath the sediments is not important: what controls the thermal behaviour is its thinness, which allows a thick layer of cold mantle to develop beneath the Moho to be subducted, and also that there should be sufficient time for this layer to develop. It seems more likely that these conditions will be satisfied by oceanic, rather than by continental, lithosphere simply because there is so much more of the former with thin crust. When the initial temperature of the oceanic lithosphere has reached a steady state before sedimentation begins, the thickness of the region whose temperature is below 600°C scarcely changes in the first 40 Ma after 25 km of sediment is added. In contrast, as Fig. 6 shows, if the plate is young and its temperature is far from steady state, and especially if the sediment contains little quartz, its subduction will not produce a slab that is seismically active to any appreciable depth. The sediments themselves are generally weak and aseismic. Therefore the seismicity is often confined to the thin pre-existing crust and the top part of the mantle below, as is the case in Figs. 1 and 2. The thermal evolution in Fig. 4 can therefore account for the presence of earthquakes beneath regions

like Vrancea, the Hindu Kush and Pamirs. Subduction of the mantle and its thin pre-existing crust within about 40 Ma of the onset of rapid sedimentation will produce a sinking slab with a thick layer of material whose temperature is below 600°C. Since the collision of India with Eurasia is believed to have occurred about 40 Ma ago, the seismic zones beneath the Hindu Kush and the Pamirs could have been produced by the subduction of such lithosphere.

The second important process is illustrated in Fig. 7. Most discussion of the origin of continental crust is concerned with its geochemistry, and how quartz-rich igneous material is produced by subduction zones. In contrast Fig. 7 shows that the thermal evolution of the crust and lithosphere converts oceanic lithosphere covered by a thick layer of sediment into a temperature structure that most geologists would recognise as Phanerozoic continental lithosphere after 200 Ma (Jaupart & Mareschal 2005). Unlike subduction zone volcanism, this process involves erosion and reworking, and conserves the continental mass. After 200 Ma has elapsed the lithospheric temperature of the mantle will exceed 600°C, and, if it is subducted, the sinking regions will be aseismic.

The last implication concerns the generation of oil and gas from thick layers of sediments deposited on old oceanic crust, a process which is now taking place in the eastern Mediterranean and Caspian Seas. Fig. 4 shows that the temperature of the sediments scarcely exceeds 100°C in the first 10 Ma while they are being deposited. During the next 10 Ma their temperature increases, mostly because of heat generated within them by radioactive decay, and reaches more than 200°C in the zone in contact with the oceanic crust. Oil is generated from organic matter as the temperature increases from about 75°C to 130°C and gas from about 100°C to 200°C (Hunt 1979 Ch 7). Because of the large thickness of the sediments involved, large quantities of both oil and gas are likely to be produced. The dip of the sediments, from the continent towards the ocean, will cause both oil and gas to migrate upwards and towards the continent. The thermal evolution in Fig. 4 can therefore account for the large accumulations of hydrocarbons in the thick sediments deposited on oceanic lithosphere by major river systems like the Niger. However, as the numerical experiments show, modelling the thermal evolution of such sediments requires the behaviour of the whole lithosphere to be taken into account, because sedimentation reduces the heat flux through the Moho by a factor of four in the reference model.

6. Conclusions

The most important result to come from the numerical experiments described above is that the deposition of a 25 km thick layer of Tertiary sediment on old oceanic crust and lithosphere has little effect on the depth to which earthquakes will occur in such lithosphere if it is subducted, leaving the sediments at the surface. Most authors (including those of this paper) had previously assumed that the low thermal conductivity of the sediments would cause the temperature of the underlying oceanic lithosphere to increase sufficiently to prevent the subducted material being seismically active. The numerical experiments show that both the history of the sedimentation and the composition of the sediments influence the thermal evolution, but that neither are likely to change this conclusion. However, if the age of the oceanic lithosphere on which the sediments are deposited is less than about 30 Ma, then its temperature will quickly increase above 600°C when it is subducted, and subduction will not produce a slab that is seismically active to depths of more than 200 km. If the seismically active zones beneath the Aegean, Caspian, Hindu Kush and the Indo-Burman Range are produced by subduction, the underlying oceanic lithosphere therefore probably formed in the Jurassic or Lower Cretaceous, and is now more than ~ 120 Ma old.

If the oceanic crust and lithosphere beneath the sediments is not removed by subduction, thermal evolution will produce a temperature structure typical of continental lithosphere whose mantle is hotter than ~ 600°C. This process takes ~ 200 Ma and only the crust will remain seismically active

when the geotherm has reached steady state.

Rapid deposition of thick layers of sediment affects the thermal structure of the entire lithosphere, and especially the heat flux through the Moho. It therefore strongly influences the thermal maturation of organic-rich source rocks that produce oil and gas.

Acknowledgements We would like to thank P. Molnar for his review. This research did not receive any specific grant from funding agencies in the public, commercial, or not-for-profit sectors.

References

Acton C.E., Priestley K., Gaur V.K., Rai S.S. 2010. Group velocity tomography of the Indo-Eurasian collision zone. *J. Geophys. Res., Solid Earth* **115** B12335. doi:10.1029/2009JB007021

Andrews, R., Rajendran, K., Rao N.R. 2020. The 4 December 2015 M_w 7.1 normal-faulting earthquake and its seismotectonic implications. *Bull. Seismol. Soc. Am.* doi:10.1785/0120190249. *Bull. Seismol. Soc. Am.*

Branlund J., Hofmeister A.M. 2007. Thermal diffusivity of quartz to $1,000°$C: effects of impurities and the $\alpha - \beta$ phase transition. *Phy. Chem. Minerals* **34** 581-595. doi:10.1007/s00269-007-0173-7

Branlund J.M., Hofmeister A.M. 2012. Heat transfer in plagioclase feldspars. *Am. Mineral.* **97** 1145-1154. doi:10.2138/am.2012.3968

Bullard E.C. 1939. Heat flow in South Africa. *Proc. R. Soc. Lond.* **A173** 474-502.

Bullard E.C. Niblett E.R. 1951 Terrestrial heat flow in England. *Mon. Notices Roy. Astron. Soc. Geophys. Suppl.* **6** 222-238.

Carslaw H.S., Jaegar J.C. 1959. *Conduction of Heat in Solids.* Oxford University Press Oxford U.K.

Chinn, D.S., Isacks B.L. 1983. Accurate source depths and focal mechanisms of shallow earthquakes in western South America and in the New Hebrides Island Arc. *Tectonics* **2** 529-563.

Christeson, G.L., Goff, J.A. & Reece, R.S. (2019). Synthesis of oceanic crustal structure from two-dimensional seismic profiles. *Rev. Geophys.* **57** 504-529. doi:10.1029/2019RG000641.

Clark S.P. 1966. Thermal conductivity. *In* Handbook of physical constants. Geological Society of America Memoir **97** 459-482.

Clauser C., Huenges E. 1995. Thermal conductivity of rocks and minerals. **In** Rock physics and phase relations: a handbook of physical constants ed. Aherns T.J. American Geophysical Union Reference Shelf **3** 105-126.

Craig, T.J., Copley, A., & Jackson, J., 2012. Thermal and tectonic consequences of India underthrusting Tibet. *Earth Planet. Sci. Lett.* **353-354**, 231-239. doi:/10/1016/j.epsl.2012.07.010

Craig T.J., Copley, A., Jackson J. 2014. A re-assessment of outer-rise seismicity and its implications for the mechanics of oceanic lithosphere. *Geophys. J. Int.* **197** 63-89. doi:10.1093/gji/ggu013.

Crosby, A., M^{c}Kenzie, D., Sclater J.G. 2006. The relationship between depth, age, and gravity in the oceans. *Geophys. J. Int.* **166** 553-573. doi:10.1111/j.1365-246X.2006.03015.x

Curray J.R. 1994. Sediment volume and mass beneath the Bay of Bengal. *Earth Planet. Sci. Lett.* **125** 371-383. doi:10.1016/0012-821X(94)90227-5

Davies J.H. 1999. A simple analytical model for subduction zone thermal structure. *Geophys. J. Int.* **139** 823-828.

Davis J.K., Lawver L.A., Norton I.O., Gahagan L.M. 2016. New Somali Basin magnetic anomalies and a plate model for the early Indian Ocean. *Gondwana Research* **34** 16-28. doi:10.1016.j.gr.2016.02.010

Emmerson B., M^{c}Kenzie D. 2007. Thermal structure and seismicity of subducting lithosphere. *Physics of the Earth and Planetary Interiors* **163** 191-208. doi:10.1016/j.pepi.2007.05.007

Engdahl, R.E., van der Hilst, R., Bulland, R. 1998. Global teleseismic earthquake relocation with improved travel times and procedures for depth determination. *Bull. Seismol. Soc. Am.* **88**, 722-743.

Frohlich C. 2006. *Deep Earthquakes.* Cambridge University Press, Cambridge, U.K.

Grose C.J., Afonso J.C. 2013. Comprehensive plate models for the thermal evolution of oceanic lithosphere. *Geochem. Geophys. Geosyst.* **14(9)** doi:10.1002/ggge.20232

Grose C.J., Afonso J.C. 2019. New constraints on the thermal conductivity of the upper mantle from numerical models of radiation transport. *Geochem. Geophys. Geosyst.* **20**. doi:10.1002/2019GC008187

Hasterok D. 2013. A heat flow based cooling model for tectonic plates. *Earth Planet. Sci. Lett.* **361**, 34-43. doi:10.1016/j.epsl.2012.10.036.

Hofmeister A.M. 2014. Thermodynamic and optical thickness corrections to diffusive radiative transfer formulations with application to planetary interiors. *Geophys. Res. Lett.* **41** 3074-3080. doi:10.1002/2014GL059833.

Hoggard M.J., Winterbourne, J., Czarnota K., White N. 2017. Oceanic residual depth measure-

ments, the plate cooling model, and global dynamic topography. *J. Geophys. Res., Solid Earth* **122** 2328-2372. doi:/10.1002/2016JB013457.

Howell, A., Jackson, J., Copley, C., McKenzie, D., and Nissen, E. 2017. Subduction and vertical motions in the eastern Mediterranean. *Geophysical Journal International* **211** 593-620. doi:10.1093/gji/ggx307.

Hunt J.M. 1979. *Petroleum geochemistry and geology.* W.H. Freeman & Co. San Francisco U.S.A.

Jaupart C., Mareschal, J.-C. 2005. Constraints on crustal heat production from heat flow data Ch. 2. **in** *The Crust* ed. R.L. Rudnick. Treatise on geochemistry Vol 3. Elsevier, Amsterdam, The Netherlands.

Katz, R.F., Spiegelman, M. & Langmuir, C.H. (2003). A new parameterization of hydrous melting. *Geochem. Geophys. Geosyst.* **4(9)**, doi:10.1029/2002GC000433.

Kojitani, H. Akaogi M. 1997. Melting enthalpies of mantle peridotite: Calorimetric determinations in the system $CaO - MgO - Al_2O_3 - SiO_2$ and application to magma generation. *Earth Planet. Sci. Lett.* **153** 209-222. doi:10.1016/S0012-821X(97)00186-6

Kufner, S.-K., and 10 others 2016. Deep India meets deep Asia: Lithospheric indentation, delamination and break-off under Pamir and Hindu Kush (Central Asia). *Earth Planet. Sci. Lett.* **435** 171-184. doi/10.1016/j.epsl.2015.11.046

Kufner, S.-K., Schurr B., Haberland C, Zhang Y., Saul J., Ischuk A. Oimahmadov I. 2017. Zooming into the Hindu Kush break-off: A rare glimpse on the terminal stage of subduction. *Earth Planet. Sci. Lett.* **461** 127-140. doi/10.1016/j.epsl.2016.12.043

Kumar A., Mitra S,, Suresh G. 2015, Seismotectonics of the eastern Himalaya and the Indo-Burman plate boundary systems. *Tectonics* **34** 2279-2295. doi:10.1002/2015TC003979

Lorinczi, P., and Houseman, G.A. 2009. Lithospheric gravitational instability beneath southeastern Carpathians. *Tectonophysics* **474** 322-336. doi:10.1016/j.tecto.2008.05.024.

McKenzie, D. 1969. Speculations on the consequences and causes of plate motions. *Geophys. J. R. Astr. Soc.*, **18**, 1-32.

McKenzie, D., Jackson J.A. and Priestley, K. 2005 Thermal structure of oceanic and continental lithosphere. *Earth Planet. Sci. Lett.*, **233**, 337-349. doi:1016/j.epsl.2005.02.005.

McKenzie D., Jackson, J., Priestley, K. 2019 Continental collisions and the origin of subcrustal continental earthquakes. *Can. J. Earth Sciences* **56**, 1101-1118. doi:10.1139/cjes-2018-0289

Mellors, R.J., Jackson, J., Myers, S., Gok, R., Priestley, K., Yetirmishli, G., et al. 2012. Deep earthquakes beneath the Northern Caucasus: Evidence of active or recent subduction in western Asia. *Bull. Seismol. Soc. Am.* **102**, 862-866. doi:10.1785/0120110184.

Mitra S., Priestley K., Acton C. Gaur V.K. 2011. Anomalous surface wave dispersion and the enigma of "continental-like" structure for the Bay of Bengal. *J. Asian Earth Sciences* **42**, 1243-1255. doi:10.1016/j.jseaes.2011.07.008

Mitra S., Priestley K.F., Borah K., Gaur V.K. 2018. Crustal structure and evolution of the eastern Himalayan plate boundary system, Northeast India. *J. Geophys. Res., Solid Earth* **123** 621-640. doi:10.1002/2017JB014714

Molnar P., Bendick R. 2019. Seismic moments of intermediate-depth earthquakes beneath the Hindu-Kush: Active stretching of a blob of sinking thickened mantle lithosphere? *Tectonics* **38** 1651-1665, doi:10.1029/2018TC005336.

Perry, M., Kakar, N., Ischuk, A., Metzger, S., Bendick, R., Molnar, P., and Mohadjer, S. 2019. Little geodetic evidence for localized Indian subduction in the Pamir-Hindu Kush of central Asia. *Geophysical Research Letters*, **46** 109-118. doi:10.1029/2018GL080065.

Press, W.H., Teukolsky, S.A., Vetterling W.T., Flannery B.R. 2007 Numerical recipes 3rd edition. Cambridge University Press, Cambridge U.K.

Rudnick R.L., Gao S. 2005. Composition of the continental crust. *in* The Crust, ed R.L. Rudnick. Treatise on Geochemistry vol. 3 pp 1-64. Elsevier Amsterdam.

Schneider, F.M., and 12 others 2013. Seismic imaging of subducting continental lower crust beneath the Pamir. *Earth Planet. Sci. Lett.* **375** 101-112. doi:10.1016/j.epsl.2013.05.015.

Sippl, C., and 12 others 2013a. Geometry of the Pamir-Hindu Kush intermediate-depth earthquake zone from local seismic data. *J. Geophys. Res., Solid Earth*, **118** 1438-1457 doi:10.1002/jgrb.50128.

Sippl, C., and 10 others 2013b. Deep burial of Asian continental crust beneath the Pamir imaged with local earthquake tomography. *Earth Planet. Sci. Lett.* **384**, 165-177, doi:10.1016/j.epsl.2013.10.013.

van Keken P., and 10 others (2008) A community benchmark for subduction zone modelling. *Physics of the Earth and Planetary Interiors*, 187-197. doi:10.1016/j/pepi.2008.04.015.

White, R., McKenzie, D. & O'Nions, R.K. (1992). Oceanic crustal thickness from seismic measurements and rare earth element inversions. *J. Geophys. Res., Solid Earth* **97**, 19683-19715.

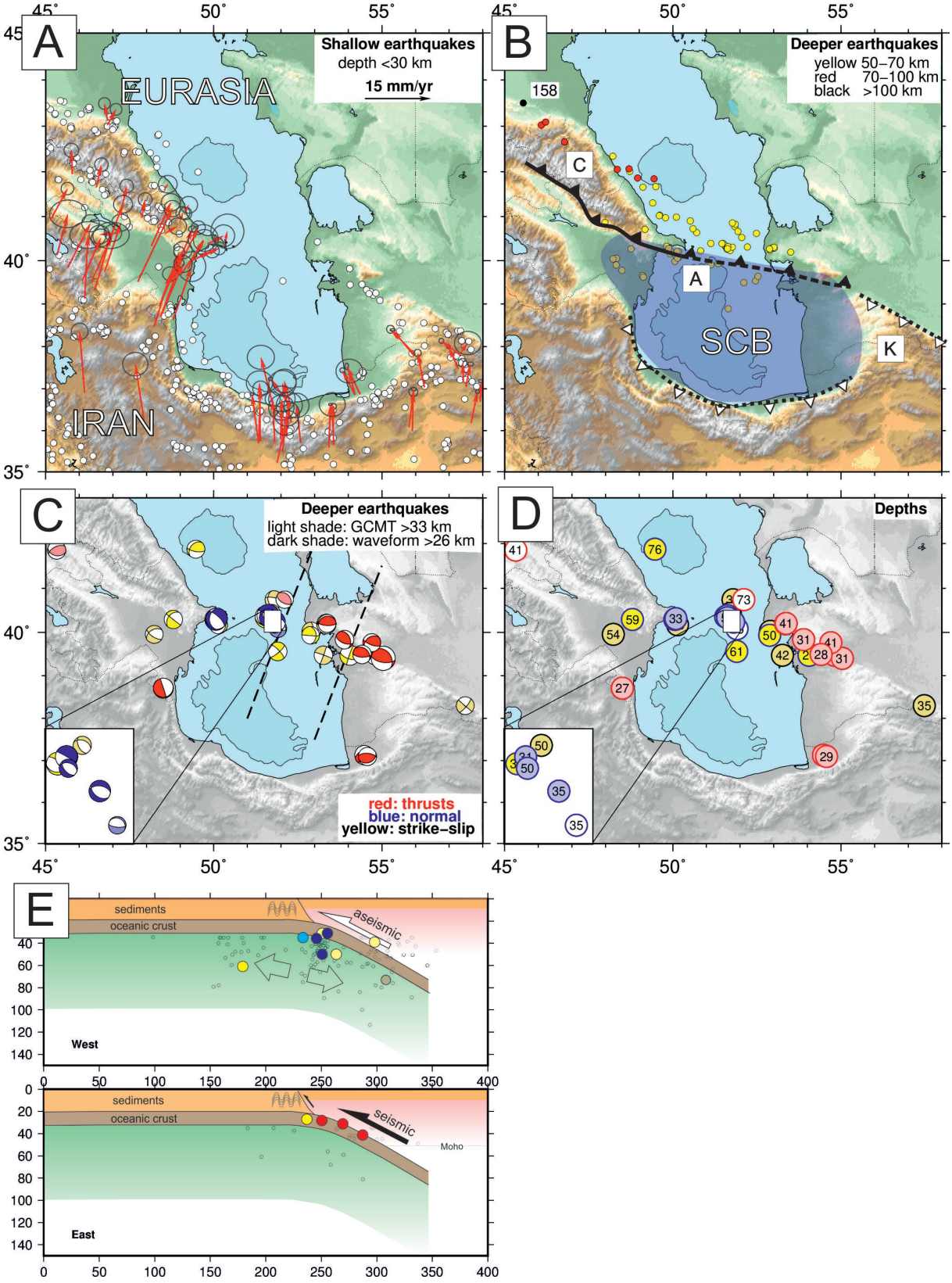
A
Shallow earthquakes
depth <30 km
15 mm/yr
EURASIA
IRAN
B
Deeper earthquakes
yellow 50–70 km
red 70–100 km
black >100 km
158
C
A
SCB
K
C
Deeper earthquakes
light shade: GCMT >33 km
dark shade: waveform >26 km
red: thrusts
blue: normal
yellow: strike–slip
D
Depths
E
sediments
oceanic crust
aseismic
West
seismic
Moho
East
45°
50°
55°
40°
35°

Figure 1:

Figure 1:(a) Seismicity, focal mechanisms, and GPS velocities with respect to Eurasia of the Caucasus (C), Apscheron Sill (A), South Caspian Basin (SCB), and Kopet Dag (K). (b) The colour of the dots correspond to different earthquake depths, taken from Engdahl et al. (1998) and later additions from the International Seismological Centre (ISC). The deepest confirmed event in the Caucasus is marked and has a depth of 158 km (Mellors et al. 2012). The polarity of the dipping seismic zone is shown by black triangles (dotted offshore) on the hanging wall. The polarity of the thrusting on the south margin of the SCB and in the Kopet Dag is shown dotted with white triangles. (c and d) Mechanisms of the shocks and earthquake depths from waveform modelling or from the centroid moment tensor (CMT) catalogue. The white insets show details within the white box on the Apscheron Sill (modified and updated from Jackson et al. 2002 and Mellors et al. 2012). (e) Cross-sections along the dashed lines in C, showing well-constrained earthquake depths, colour-coded by mechanism as in C and D, consistent with known sediment thickness and Moho depths (see Jackson et al 2002). In the east, the presumed subduction interface is seismically active at about 40 km depth; in the west it is aseismic while extensional earthquakes, presumably associated with bending, occur in the down-going lithosphere.

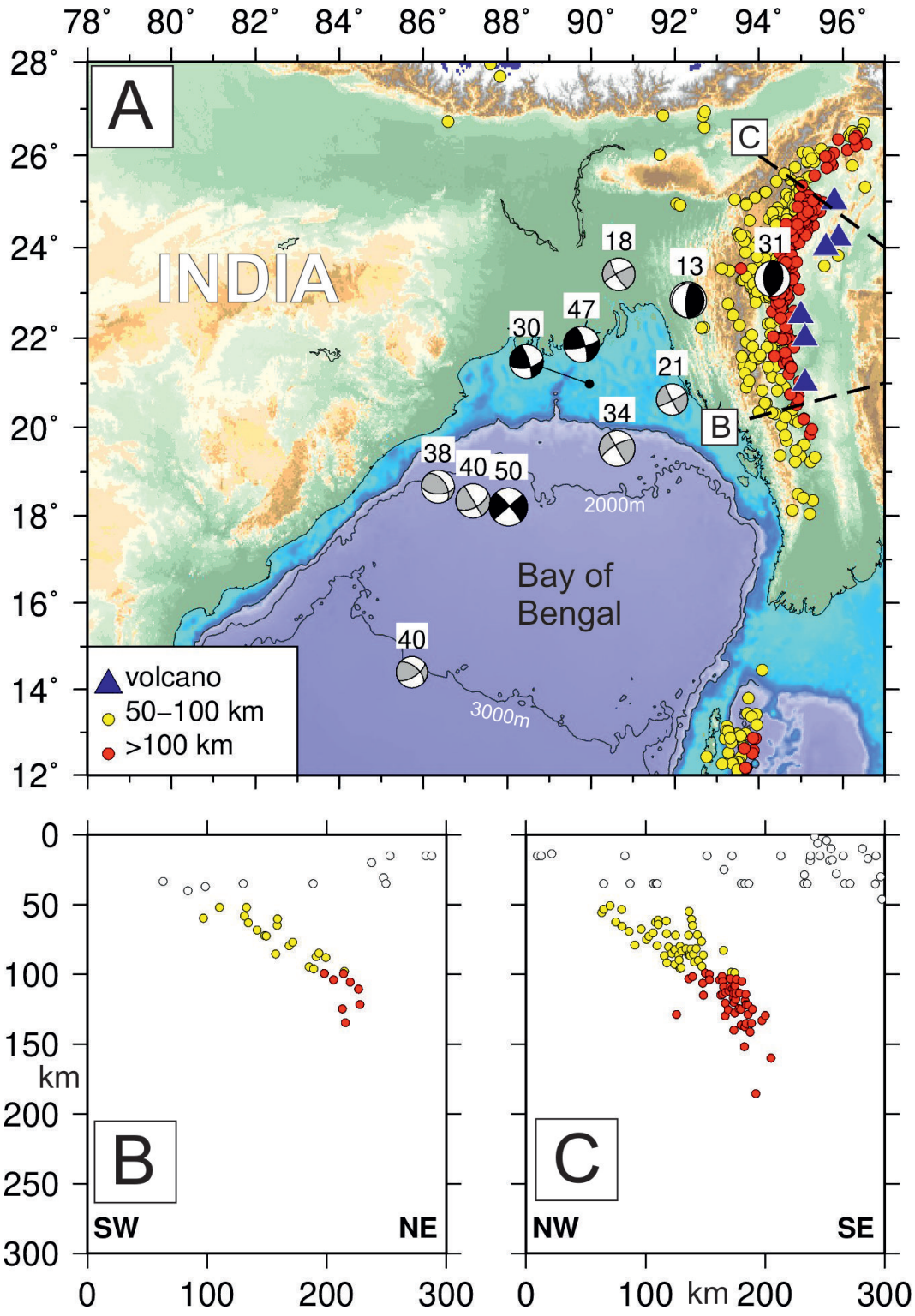

Figure 2: (a) Earthquake focal mechanisms determined from teleseismic waveform modelling (black) or taken from the global CMT catalogue (grey) in the Bay of Bengal, with two thrusts shown in the Indo-Burman ranges (the numerous strike-slip events have been omitted: see Kumar et al 2015). Centroid depths in km are in white boxes, determined from waveform modelling (black) or taken from Engdahl et al (1998) and later additions from the ISC. Epicentres of earthquakes deeper than 50 km are from Engdahl et al (1988). (b and c) Cross-sections showing seismicity in the Indo-Burman subducting slab. The source parameters of the earthquakes with fault-plane solutions are given in the Supplementary Material.

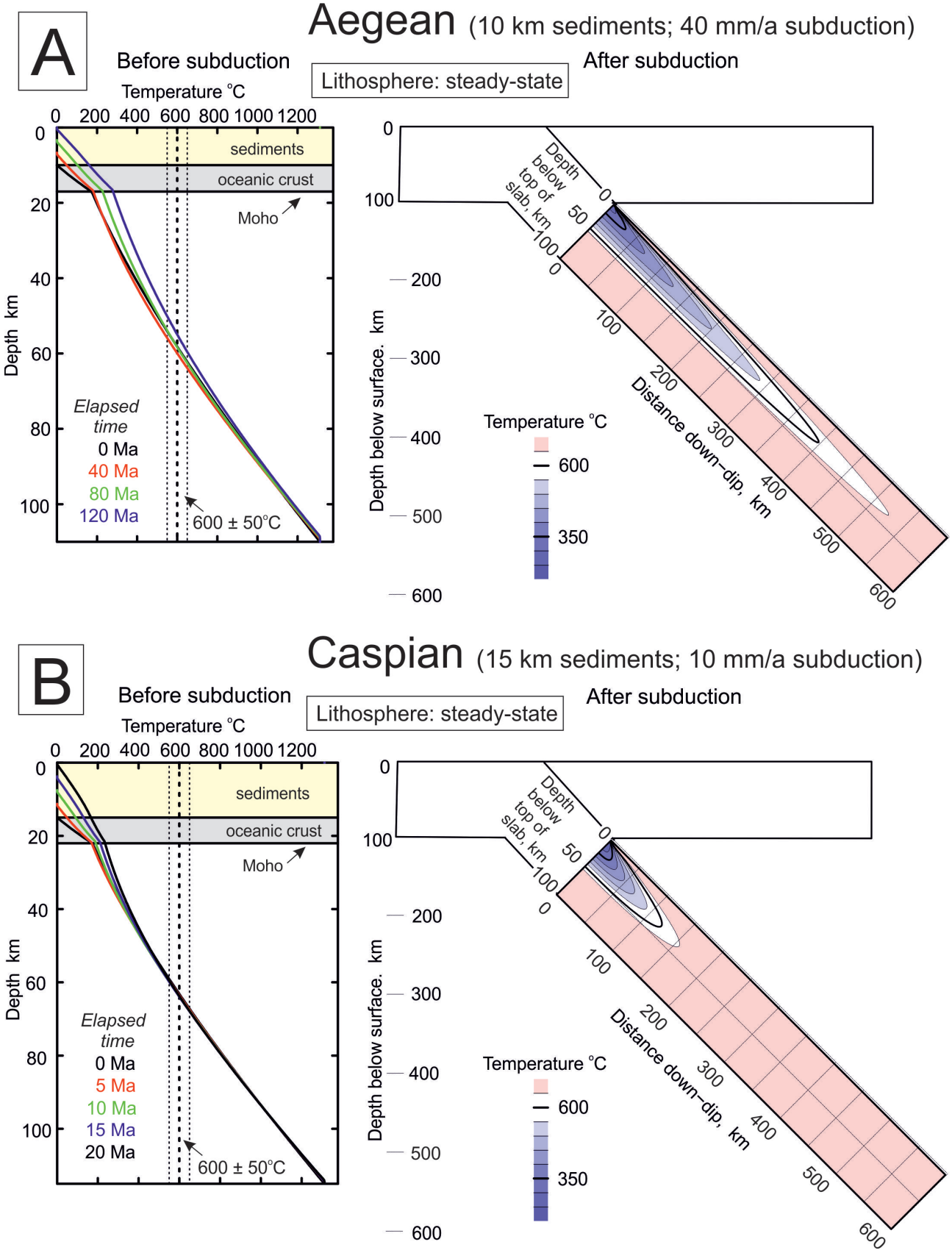

Figure 3: Thermal models of the development of the Aegean and Caspian subduction zones.

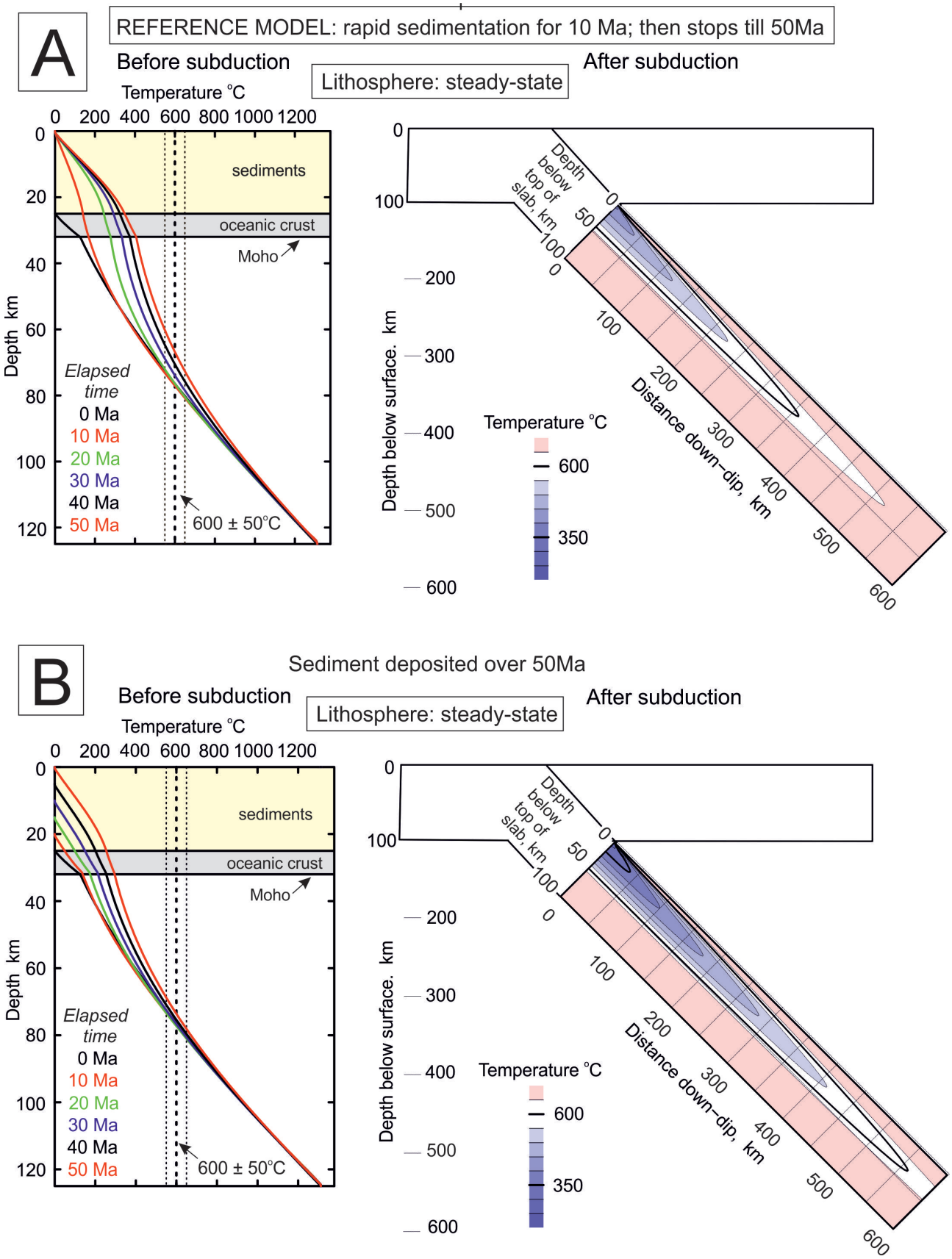

Figure 4: Reference model (a), with 25 km of sediment, whose thermal conductivity is 2.8 W m^{-1} $°C^{-1}$, deposited on old oceanic lithosphere in 10 Ma, and subducted at 50 mm/a 50 Ma after the start of sedimentation. (b) As above, except sedimentation lasts for 50 Ma.

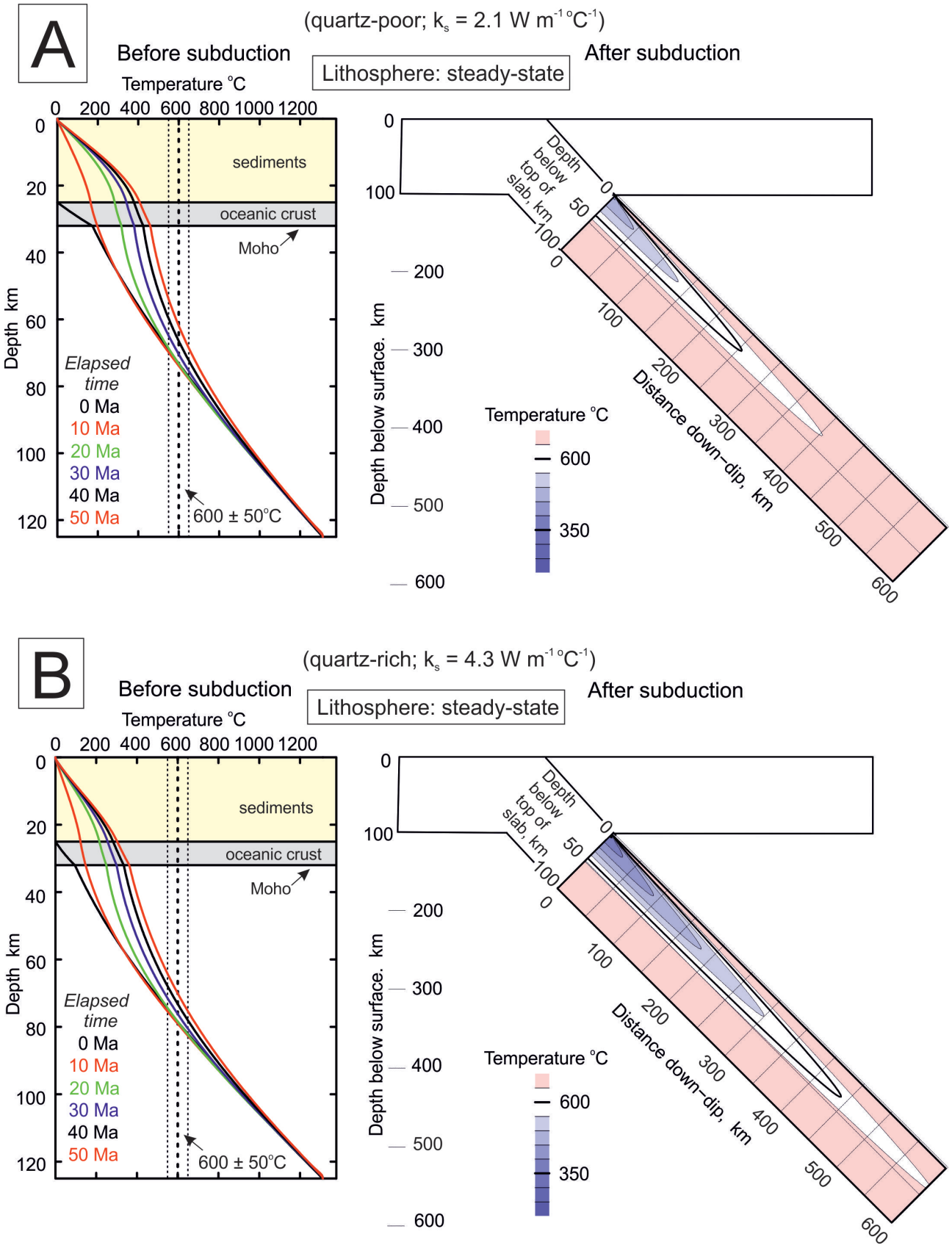

Figure 5: As for the reference model, except the thermal conductivity of the sediments is 2.1 W m^{-1} °C^{-1} in (a), and 4.3 W m^{-1} °C^{-1} in (b).

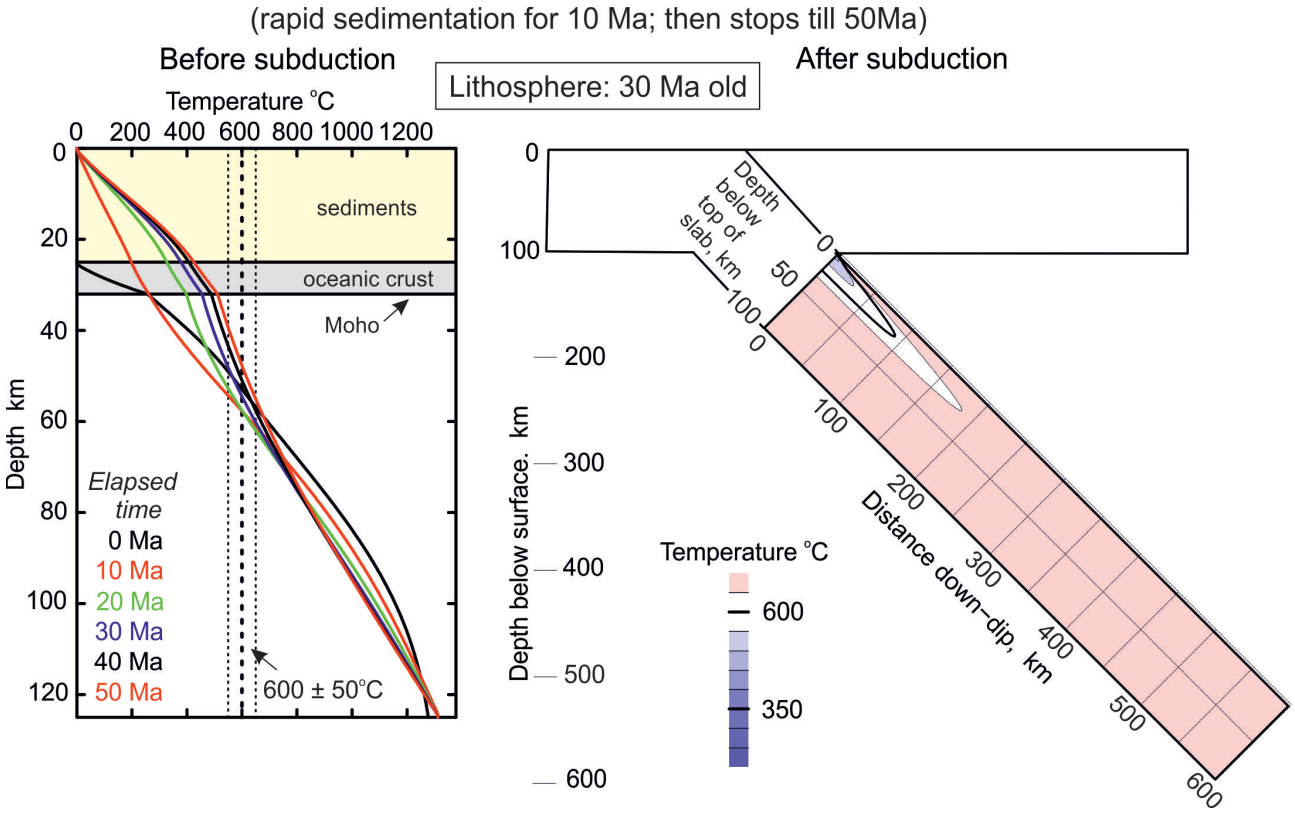

Figure 6: As for the reference model, but with the sediments deposited on 30 Ma old oceanic lithosphere.

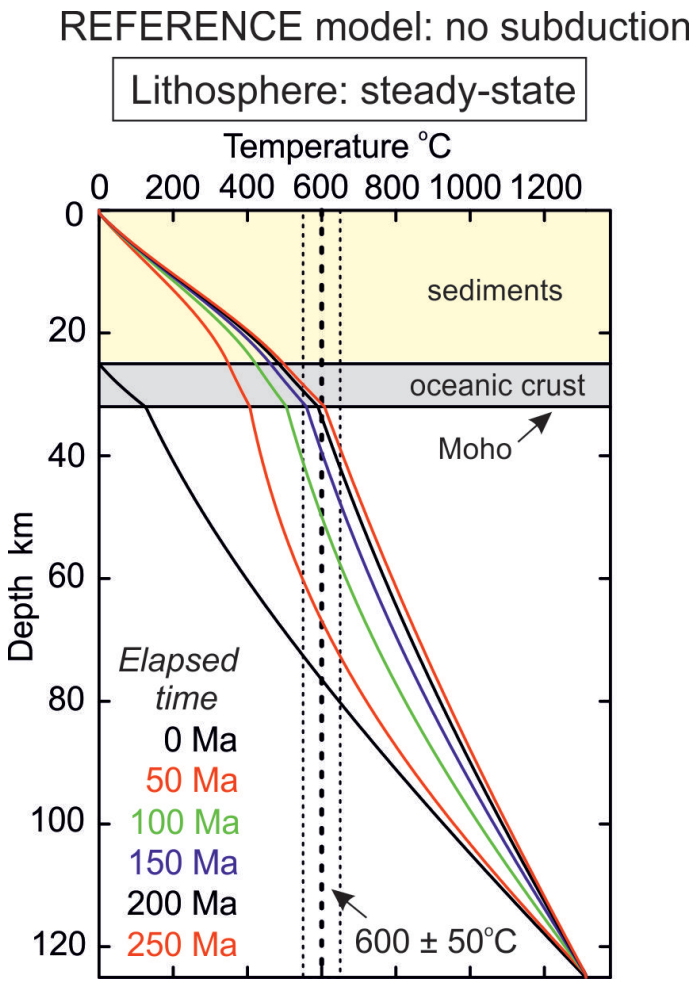

Figure 7: Temperature profiles for the reference model when no subduction occurs.

Supplementary Material

The supplement consists of three parts. The first concerns the numerical scheme used to solve the heat flow equation in the sediments, the first step. It differs from that used by M^{c}Kenzie et al. (2005) because it includes an advective, as well as a diffusive, term, and takes account of the discontinuity at the Moho. The second part uses the waveforms of earthquakes beneath the Bengal Fan to determine their depths. The third part uses the waveforms of earthquakes from a large earthquake on the Antarctic plate to determine its depth and details of its rupture propagation.

1. Numerical Scheme

The variation of ρ and C_p with temperature is small compared with that of κ and k. It is therefore convenient to rewrite equation (3) as

$$\frac{\partial T}{\partial t} = \frac{\partial}{\partial z}\left(\kappa \frac{\partial T}{\partial z}\right) - u\frac{\partial T}{\partial z} + \frac{H}{\rho C_p} + E(z,t) \tag{A1}$$

and

$$E(z,t) = \frac{1}{\rho C_p}\left[-T\frac{\partial(\rho C_p)}{\partial t} + \left(\kappa\frac{\partial T}{\partial z} - uT\right)\frac{\partial(\rho C_p)}{\partial z}\right] \tag{A2}$$

and to treat E as a small perturbation, solving equation (A1) by iteration. This correction produced trivial changes to the thermal evolution and was therefore ignored. The nonlinear term in equation (A1) can be written as

$$\frac{\partial^2 F}{\partial z^2}$$

using the expression for $\kappa(T)$

$$F = \int \kappa(T)dT = aT - cb\exp(-T/c) - de\exp(-T/e) \tag{A3}$$

It is also convenient to rewrite equation (A1) in dimensionless form, using the values of κ, ρ and C_p when $T = 0°$C, κ_0, ρ_0 and C_0, the thickness of the oceanic lithosphere a, and the temperature at the base of the lithosphere T_p

$$z = az', \quad t = \frac{a^2}{\kappa_0}t', \quad T = T_pT', \qquad H = \frac{\kappa_0\rho_0 C_0 T_p}{a^2}H', \quad F = \kappa_0 T_p F'$$

giving

$$\frac{\partial T'}{\partial t'} = \frac{\partial^2 F'}{\partial z'^2} - Pe_c\frac{\partial T'}{\partial z'} + H' \tag{A4}$$

where the thermal Peclet number Pe_c is ua/κ_0. Equation (A4) can then be solved using a modified Crank-Nicholson scheme. Omitting primes, an implicit finite difference approximation to equation (A4) is

$$\frac{T_i^{n+1} - T_i^n}{\Delta t} = \left[\left(F_{i+1}^{n+1} - 2F_i^{n+1} + F_{i-1}^{n+1}\right) + \left(F_{i+1}^{n} - 2F_i^{n} + F_{i-1}^{n}\right)\right]/(2\Delta z^2)$$

$$-Pe_c\left[\left(T_{i+1}^{n+1} + T_{i-1}^{n+1}\right) - \left(T_{i+1}^{n} + T_{i-1}^{n}\right)\right]/(4\Delta z) + H_i \tag{A5}$$

where T_i^n is the value of $T(n\Delta t, i\Delta z)$ and similarly for F, κ, k and H. Equation (A5) is centred on $(n + 1/2)\Delta t$ in time and $i\Delta z$ in space. If κ is constant this equation is stable for all values

of Δt, though it is only accurate if $\Delta t <$ both Δz^2 and $\Delta z/Pe_c$. F_i^{n+1} can be written in terms of T and κ using a Taylor expansion

$$F_i^{n+1} = F_i^n + (T_i^{n+1} - T_i^n)\kappa_i^n \tag{A6}$$

Equation (A5) can be then rewritten in a form that can be solved by tridiagonal elimination

$$AT_{i-1}^{n+1} + BT_i^{n+1} + CT_{i+1}^{n+1} = R \tag{A7}$$

where

$$f_a = \frac{\Delta t}{2\Delta z^2} \ , \qquad f_b = \frac{Pe_c \Delta t}{4\Delta z}$$
$$A = -f_a\kappa_{i-1}^n - f_b \ , \quad B = 1 + 2f_a\kappa_i^n \ , \quad C = -f_a\kappa_{i+1}^n + f_b \ ,$$
$$R = T_i^n + 2f_a(F_{i+1}^n - 2F_i^n + F_{i-1}^n) - f_a(\kappa_{i+1}^n T_{i+1}^n - 2\kappa_i^n T_i^n + \kappa_{i-1}^n T_{i-1}^n)$$
$$-f_b(T_{i+1}^n - T_{i-1}^n) + H_i\Delta t \tag{A8}$$

and $H_i = 0$ except in the sediments. The boundary conditions $T(0) = 0.$ and $T(1) = 1$ were imposed by setting the first and the last values of T on the grid to these values. Once sedimentation stops, both the Peclet number and f_b are set to zero. These expressions are valid when the three points $i-1,\ i,\ i+1$ are all either in the mantle or in the crust. Dealing with the discontinuity in material properties at the Moho is more complicated. It was handled by placing the discontinuity at the nearest mesh point i and using the conservative form of equation (A4) to calculate the conductive and advective flows across boundaries at $i-1/2$ and $i+1/2$, centred in time at $n+1/2$. Defining

$$G^n(c) = \left[G_{i-1}^n(c) + G_i^n(c)\right]/2 \ , \quad G^n(m) = \left[G_i^n(m) + G_{i+1}^n(m)\right]/2 \ ,$$

$$\overline{G^n} = \left[G_i^n(c) + G_i^n(m)\right]/2$$
$$k^n(c) = \left[k_{i-1}^n(c) + k_i^n(c)\right]/2 \ , \quad k^n(m) = \left[k_i^n(m) + k_{i+1}^n(m)\right]/2 \ ,$$

where (c) is the value in the crust and (m) that in the mantle, and

$$g_a = \frac{\Delta t}{2\overline{G^n}\Delta z^2} \ , \qquad g_b = \frac{Pe_c \Delta t}{4\overline{G^n}\Delta z}$$

gives

$$A = -g_a k^n(c) - g_b G^n(c) \ , \quad B = 1 + g_a\left[k^n(c) + k^n(m)\right] + g_b\left[G^n(m) - G^n(c)\right] \ ,$$

$$C = -g_a k^n(m) + g_b G^n(m) \ ,$$
$$R = T_i^n + g_a\left[k^n(m)(T_{i+1}^n - T_i^n) - k^n(c)(T_i^n - T_{i-1}^n)\right]$$
$$+g_b\left[G^n(c)(T_i^n + T_{i-1}^n) - G^n(m)(T_{i+1}^n + T_i^n)\right] \tag{A9}$$

If κ and G are constant and are the same in both the crust and mantle, then $\kappa = k/G$ and $F = \kappa T$. Substitution into equations (A8) and (A9) then gives the same expressions for A, B, C and R in each case, showing that equation (A9) neglects the variation of κ with temperature for the mesh point centred on the Moho. A value of Δz of 0.005 was used, partly to minimise the resulting error.

2. Earthquake source parameters

The fault-plane solutions and depths of earthquakes shown in Fig. 2, and their sources, are listed in Table 1. Body-wave modeling was carried out in the manner described by Kumar et al. (2015). New solutions for three earthquakes are shown in Figs. 1–3.

Date *DaMoYr*	*Time* *HrMnSc*	*Long.*	*Lat.*	*Strike*	*Dip*	*Rake*	M_w	*Depth (km)* *PSH*	*EHB*	*Mechanism*
080482	024119	86.35	18.66	325	51	131	5.2		38	CMT
040782	183427	90.62	19.53	240	73	0	5.6		34	CMT
010785	022352	87.19	18.34	60	58	1	5.4		40	CMT
120689	000410	89.77	21.86	343	75	167	5.6	47		PSH/Fig.S3
090792	213401	89.96	20.98	79	59	13	5.3	30		CMT/Fig.S2
260703	231818	92.31	22.85	338	32	82	5.6	13		PSH/Kumar (2015)
270703	120729	92.34	22.83	2	16	88	5.4	13		PSH/Kumar (2015)
110506	172254	94.32	23.31	15	42	102	5.6	31		PSH/Kumar (2015)
300506	194345	91.93	20.63	63	85	-2	4.9		21	CMT
100910	172416	90.66	23.41	149	77	171	5.1		18	CMT
210514	162154	88.03	18.20	319	84	180	6.0	50		PSH/Fig.S1
120219	013227	85.73	14.40	310	58	150	4.9		40	CMT

Table 1: Source parameters and depths of earthquakes whose fault-plane solutions are shown in Fig. 2. Depths are determined from P and SH body-wave model-ling (PSH) or from the updated catalogue of Engdahl et al. (1998). Focal mechanisms are determined either from body-wave model-ling (PSH) or are taken from the gCMT catalogue (www.globalcmt.org)

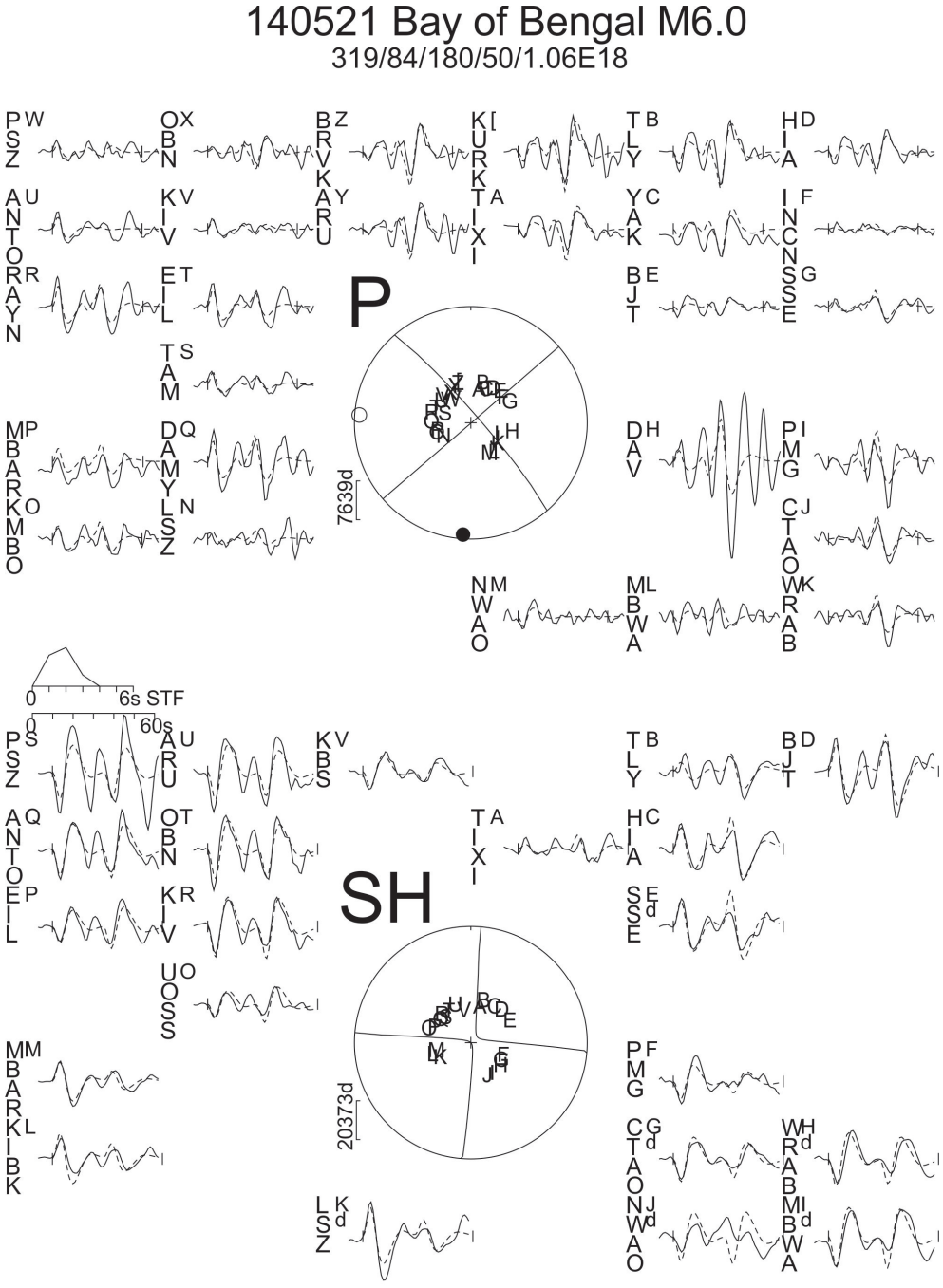

Figure 1: P (top) and SH (bottom) nodal planes and waveforms (observed, solid; synthetic, dashed) for the 21 May 2014 earthquake in the Bay of Bengal. Numbers beneath the heading are strike/dip/rake/centroid depth/moment. The station code for each waveform is accompanied by a letter identifying its position on the focal sphere, arranged clockwise alphabetically. The time window used for the inversion is marked by vertical bars on each waveform. P and T axes are solid and open circles on the P focal sphere. STF is the Source Time Function.

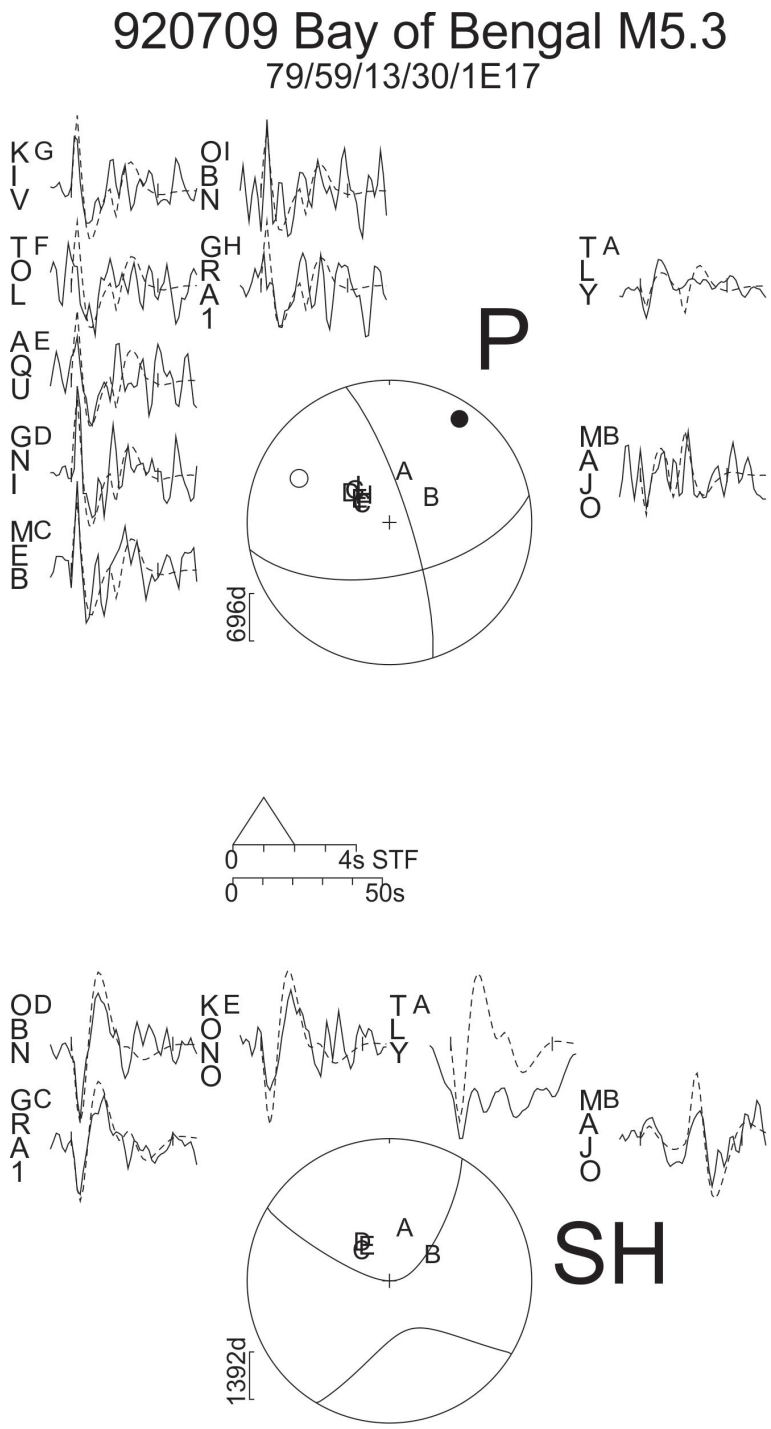

Figure 2: P (top) and SH (bottom) nodal planes and waveforms for the 9 July 1992 earthquake in the Bay of Bengal. There is an insufficient distribution of stations to independently constrain the fault-plane solution, which is that of the gCMT. The P waves are not very sensitive to the depth because the pP and sP raypaths depart along nodal planes. But the SH waveforms are more sensitive, and the separation of sS is clearly visible, particularly at MAJO, constraining the depth to ∼30 km.

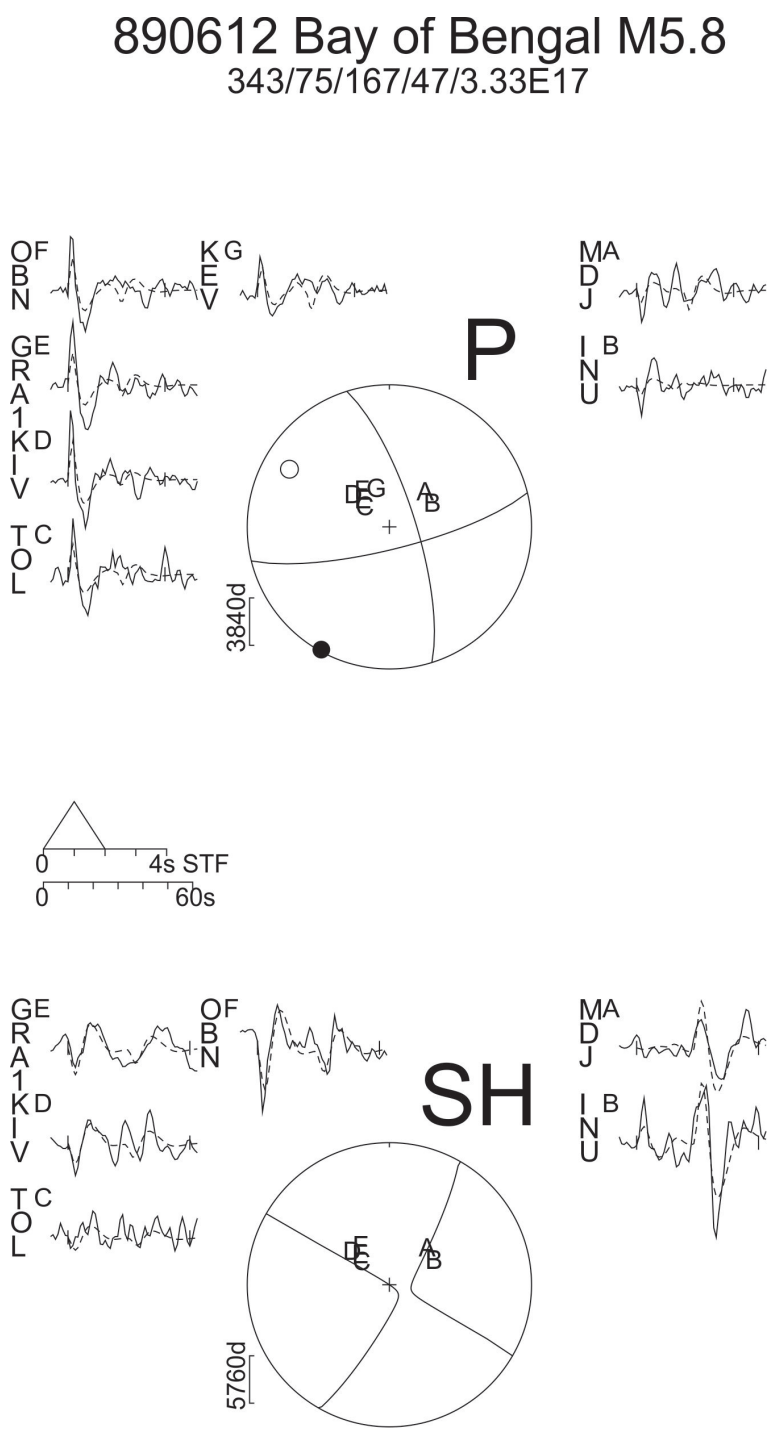

Figure 3: P (top) and SH (bottom) nodal planes and waveforms for the 12 June 1989 earthquake in the Bay of Bengal. The depth is well constrained at ∼47 km by the clearly visible separation of sS, particularly at INU, MDJ and OBN.

3. The Antarctic Plate earthquake of 4 December 2015 (Mw 7.1)

On 4 December 2015 an earthquake of Mw 7.1 occurred in the Antarctic plate 500 km SW of the Southeast Indian Ridge in lithosphere 20–25 Ma old. Andrews *et al.* (2020) claimed this event had a centroid depth of 34 km, deeper than the 800°C isotherm. They based their argument on a finite-source fault model, using teleseismic P and SH waveforms. Several aspects of the analysis they presented caused us to also examine this earthquake ourselves. Our concerns were, briefly:

(a) Aspects of the finite-source method and results:

- The fault grid in the inversion of Andrews *et al.* consists of 8×8 km^2 squares, and they solve for the slip at the nodes. It is unclear whether this really gives the resolution that is claimed: especially for an event of only Mw 7.1, which is small for such a finite-source analysis and only likely to have a source dimension of about 40–50 km.

- Several of the results they presented were puzzling: (i) the source time function was 40 seconds long (their Fig. 4c), which is very long for an event of only Mw 7.1; (ii) the maximum slip was only 1.06 m and the average only 0.12 m: these are very low values for an earthquake of Mw 7.1.

- Superficially, the misfit plot (their Fig. 3d) is quite convincing, but it is unclear how shallow the minimum really is.

- There is little discussion of the trade-offs between source parameters that are inevitable in such finite-source inversions, especially between depth, rupture velocity, source dimension and duration.

- The results of the inversion are dominated by a single circular slip patch on the fault, but it is unclear how well its dimensions are resolved, given the smoothing inherent in both the inversion routine and the frequency content of the data.

(b) Other technical considerations:

- Andrews *et al.* used stations out to 100° epicentral distance: yet beyond 90° (80° for S) interference from core phases that arrive within a few seconds of direct P and SH is important when the source duration is likely to be 10 s or more. Indeed, of their 58 P waveforms, 25 of them were beyond 90°, and of their 39 SH waves, at least 2 were beyond 90° (and these 2 are the only stations at a crucial azimuth: see below).

- Their inversion for a source time function (STF), using 10 triangles of 3 s overlapping by 1.5 s, gives a total possible duration of 16.5 s. It is therefore unclear how they obtained a duration of 40 s (their Fig. 9d).

- With 58 P and 39 SH waveforms there would normally be a good chance of breaking the usual trade-offs between depth, STF and Mo. But close inspection of their Fig. 5 and of the azimuths to the stations (the number after the station code), reveals that of the 39 SH: 7 are in the azimuth range 086–100 (west Pacific); 28 are in the azimuth range 144–190 (Antarctica); 2 are in direction ∼060 (both beyond 90° distance); 1 (Macquarie) at azimuth 127, and 1 at 274 (Africa). There are **no** SH waveforms at all in the azimuth

range 277–127: i.e. all the SH stations are in the south and none are to the north. This matters, because the trade-offs will be bad, and as for resolving the claimed N-S rupture propagation, impossible: the biggest effects by far are in the azimuth of SH and if only one direction is illuminated, you just can't tell.

- The SH are down-weighted relative to P by 0.1. This is an unusually large difference, demoting the influence of the phase best able to resolve azimuthal directivity.
- Their Fig. 5, which shows the fits of synthetic to observed seismograms, is scaled to a uniform peak-amplitude, so all information about real relative amplitudes and sensitivity is lost.

We therefore performed some analysis ourselves, using the MT5 inversion program used in section 2 of the Supplementary Material above and described in detail by Kumar *et al.* (2015).

3.1 The best centroid solution (Fig. 4)

This has a much better station distribution, especially for SH (and all in the distance range 30-90°), than the analysis of Andrews *et al.* The source time function was defined by 10 elements with half-duration 3 s, overlapping by 3 s, giving a total possible duration of 33 s; but the last few elements were all near-zero, and the STF is only 20 s long. We used a velocity model with 7 km of crust (Vp=6.8 km/s, Vs=3.9 km/s) over a mantle half-space of Vp=8.1 km/s, Vs=4.5 km/s, with 3.5 km water depth. The best-fit centroid depth is 15 km, and is measured from the sea surface (11.5 km below the sea bed). This depth, and the normal-faulting mechanism, are both extremely stable, converging to this result from widely differing starting positions. The nodal planes are very well constrained, and the mechanism (034/44/288 for strike/dip/rake) is not significantly different from the Global CMT solution (042/47/302). The relative amplitudes are real (though are displayed, corrected for geometrical spreading, as though at the same epicentral distance to reflect true amplitude variations related to the radiation pattern). The advantage of using real, not scaled, amplitudes is illustrated by the very small SH at CHTO in the north, requiring it to be near a nodal plane for SH and its surface reflection. (Recall that Andrews *et al.* had no SH at all in the northern hemisphere). The fit for P and SH is reasonable, but there are some systematic effects. In particular the SH wavelets in the NNE e.g. (JAGI, MMRI, PMG, WRAB) are all slightly too narrow (the downward peak is too early). In the other direction, to the SSW, the wavelet at SNAA is too broad. This might be effect of rupture propagation, since whichever plane is the fault plane, the fault must strike approximately NNE-SSW. So we looked at this next.

3.2 Effects of rupture propagation. (Figs. 5 and 6)

We added the effect of a line source propagating either to the SSW or to the NNE at 2.7 km/s (a fairly typical value, and the one used by Andrews *et al.*). Fig. 5 illustrates the effect using 6 stations (3 P in black, 3 SH in red) at azimuths to the NNE (KAPI, MMRI), SSW (SNAA) or to the side (TAU, ATD). The top line is the centroid solution from Fig. 4. We fixed the strike, dip, rake, and left the STF and Mo free in the next inversions.

Line 2 is for a rupture propagating to the SSW. As expected, the SH wavelet is broadened at MMRI (NNE) and narrowed at SNA (SSW), improving the fits, and there is no effect to the side (ATD). The effect is greater for SH than for P, but notice the fit also improves for P, because the broader wavelet to the NNE (KAPI) shows a double-upward pulse, which is better separated than in the narrower pulse to the SSW (SNAA), and both azimuths are better fitted. Again, there is no effect to the side (TAU).

Line 3, by contrast, includes a rupture propagating NNE, where the same effects produce dramatically worse fits.

Note also that each inversion produces a slightly different depth, which was left as a free parameter. The propagation to the SSW (line 2) needs a slightly shorter time function overall, and so has a slightly deeper depth to make up the wavelet width: a classic trade-off. The moment is about the same. The depth moves from 15 km (centroid) to 21 km (line source to the SSW). The fit for all stations, from the inversion of line 2 showing the best SSW-propagating source, is shown in Fig. 6.

3.3 Resolution of centroid (or line source) depth (Fig. 7)

The SSW-propagating line source (Fig. 6) is clearly the best fit to the waveforms. This is not a surprise: this size of Mw 7.1 is about when such effects are expected, because the source no longer looks like a point source in the bandpass we use, which is the response of the old WWSSN 15-100 instrument (see e.g. Yielding *et al.* 1981). The best test for depth resolution is to fix the depth at various values, leaving all other parameters free, and see if the trade-offs can manage the fit as well. This is shown in Fig. 7, using 3 P stations (black) and 3 SH (red), chosen carefully so their reflected phases do not lie on nodal planes. The value at which depth was fixed is shown in red (in km), varying from 11 to 35 (Andrews *et al.* got 34 km). The formal best fit, with the smallest misfit, is at 22 km (Fig. 6), and waveform fits at other depths that are noticeably worse are marked with a cross. Note that as depth increases (top to bottom) the STF gets shorter (from 35 to 16 s), and the moment decreases (from 6.3×10^{19} to 3.0×10^{19} Nm): again, a classic trade-off, with the moment increasing at shallow depths because P and pP have opposite polarities and start to cancel each other out for dip-slip faulting. The inversion tries to maintain the wavelet (pulse) width by adjusting either the STF or the depth, but the trade-off is not complete, because whereas the STF duration affects P and SH the same, the depth does not, because Pp-P and sS-S delays do not change in quite the same way with depth. The misfit minimum is fairly broad and a range of 22 ± 5 km is acceptable. These are values below the sea surface (water depth 3.5 km): so the depth is about 19 ± 5 km below the sea bed. The values of 34 km from Andrews *et al.*, and 29 km from global CMT, are both too high.

3.4 Source dimensions.

An estimate of the fault length is the STF duration times the rupture velocity, Vr (with obvious trade-offs between the two). In this case the best STF (Fig. 6) is about 20 s with Vr of 2.7 km/s; which gives a fault length of 54 km — quite reasonable for Mw 7.1.

The moment value of 6×10^{19} Nm is quite stable, and the same as the global CMT solution. From the expression for Mo, we can now estimate the fault width W, where:

$$Mo = \mu A\bar{u} = \mu LW(\alpha L),$$

with L = fault length, A = fault area, W = down-dip fault width, $\bar{u}$ = average slip, $\mu = 3\times10^{10}$ Nm^{-2}, and $\alpha = \bar{u}/L = 5\times10^{-5}$ (a typical value, equivalent to a stress drop of 1.5 MPa). This gives a value for W of 12 km, and an expected average slip (αL) of about 3 metres: all perfectly sensible, ordinary values for an earthquake of Mw 7.1.

By contrast, the solution of Andrews *et al.* had an average slip of 0.12 m on a square fault of dimension 48×48 km^2, which would have a stress drop of 0.08 MPa. Those slip and stress-drop values would be extraordinary for a Mw 7.1 earthquake.

3.5 The 800°C isotherm.

The down-dip width of 12 km on a fault dipping 45° gives a vertical depth extent of faulting of about 10 km: i.e. ±5 km either side of the centroid (line) source depth. For the best-fit depth of 22 km this means a depth extent of faulting between 17 and 27 km. To this we should add ±5 km for errors. Again these are values below the sea surface; so this means 14–24 km (±5) below the sea bed. Those ranges are shown in Fig. 8, adapted from Craig *et al.* (2014): the yellow circle is the best depth; white is the vertical extent of faulting, with black errors). The centroid is well above the 600° isotherm and, even allowing for errors, the deepest penetration of rupture is above the 700°C isotherm. Note that, with SH only to the south, and ray paths all downward along the fault, Andrews *et al.* had no realistic chance of resolving vertical propagation effects or the vertical extent of slip from directivity in their finite-source model. Directivity effects are always far greater with azimuth (i.e. horizontal propagation), and that could not be resolved either, since all their illumination is from one direction.

3.6 Conclusion.

We conclude that there is no evidence that the centroid of the 2015 Antarctic plate earthquake is deeper than the 600°C isotherm, and that rupture is unlikely to have penetrated deeper than about 600-650°C. This earthquake is consistent with the worldwide pattern documented (with much more data) by Craig *et al.* (2014).

Additional reference:

Yielding, G., Jackson, J.A., King, G., Sinvhal, H., Vita-Finzi, C. & Wood, R.. 1981. Relations between surface deformation, fault geometry, seismicity and rupture characteristics during the El Asnam (Algeria) earthquake of 10 October 1980. *Earth. Planet. Sci. Letts.*, **56**, 287–304.

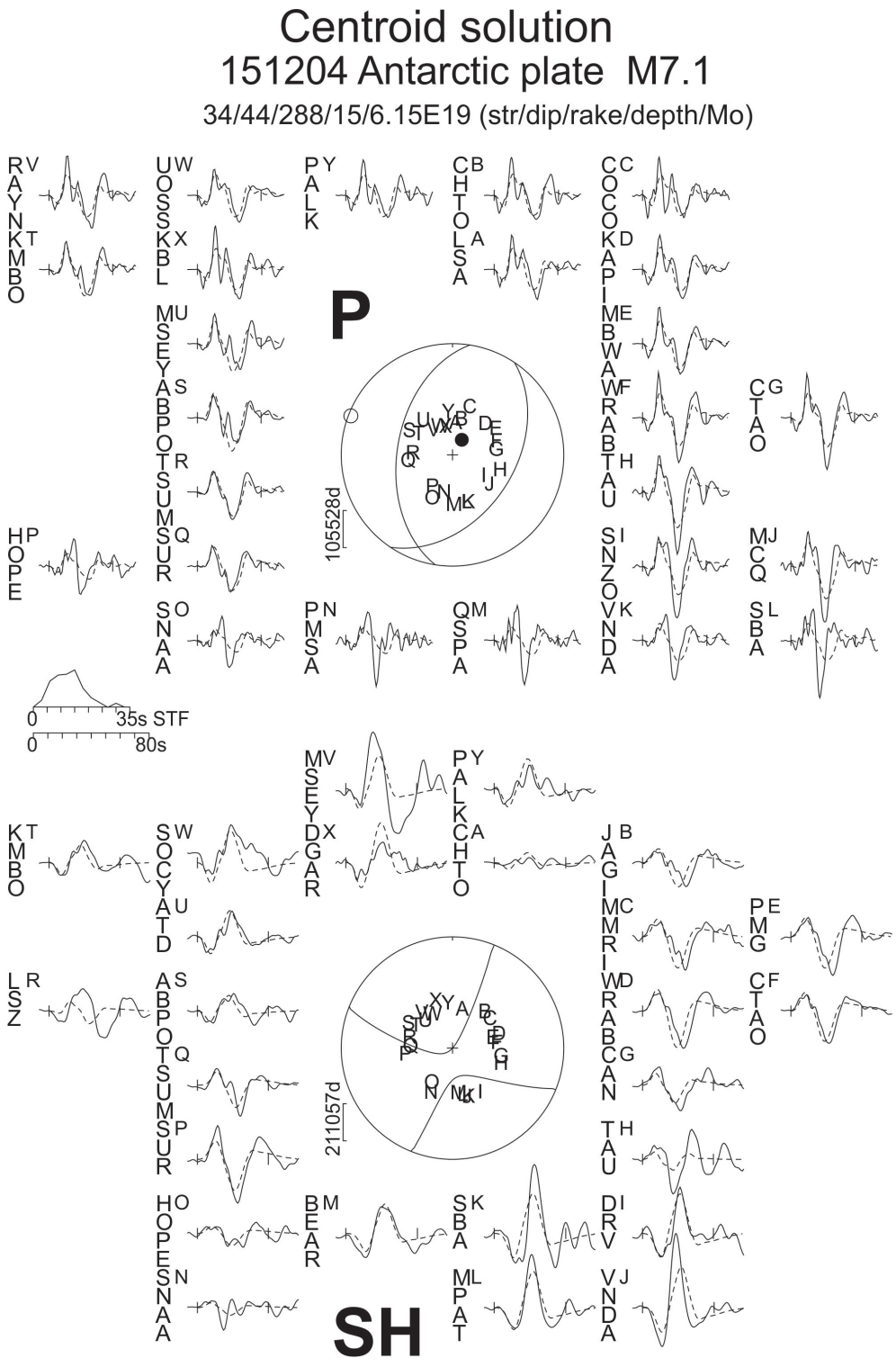

Figure 4: Centroid solution for the 2015 Antarctic plate earthquake. Format and symbols as in Fig. 1.

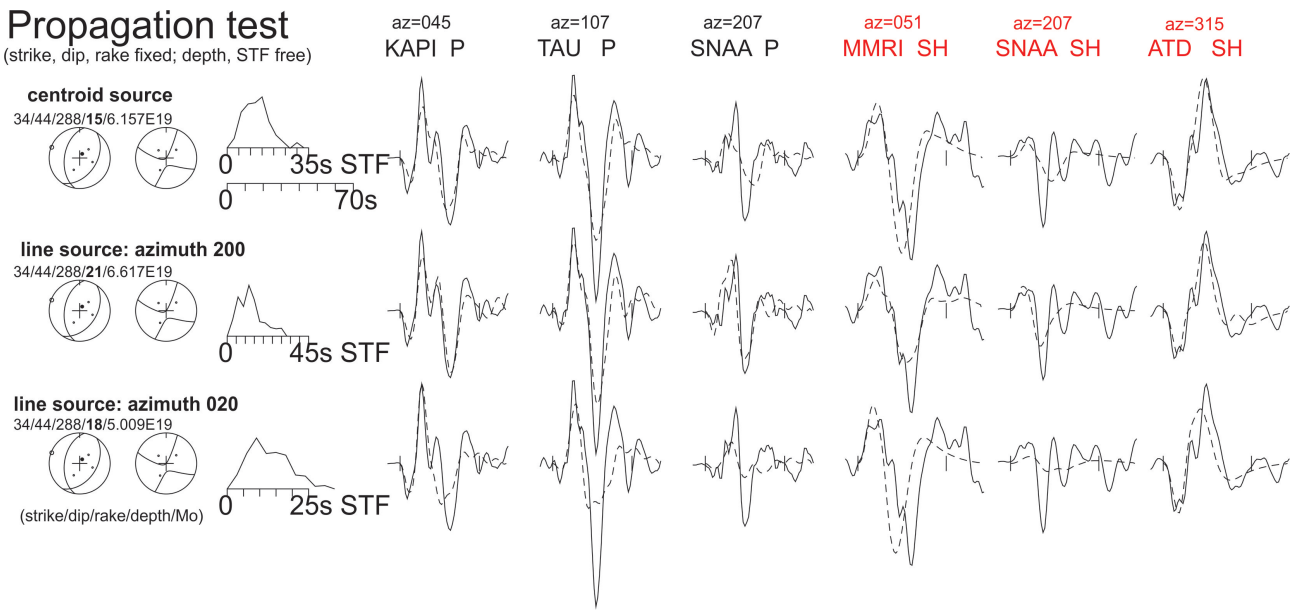

Figure 5: Illustration of the effects of rupture propagation to the SSW (line 2) and NNE (line 3), compared with the centroid solution of Fig. 3 (line 1). See text for details.

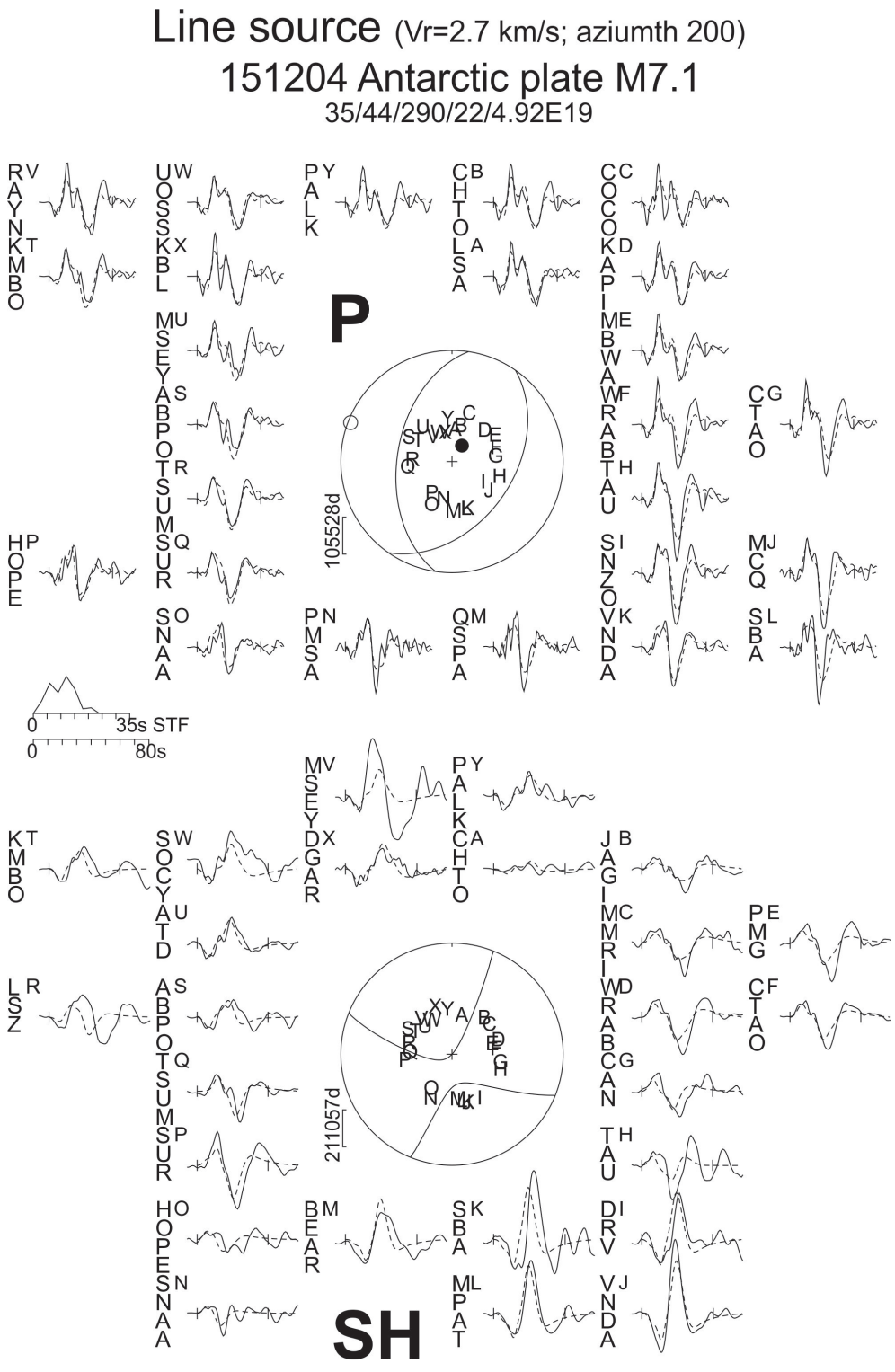

Figure 6: Solution for the SSW-propagating line source. See text for details.

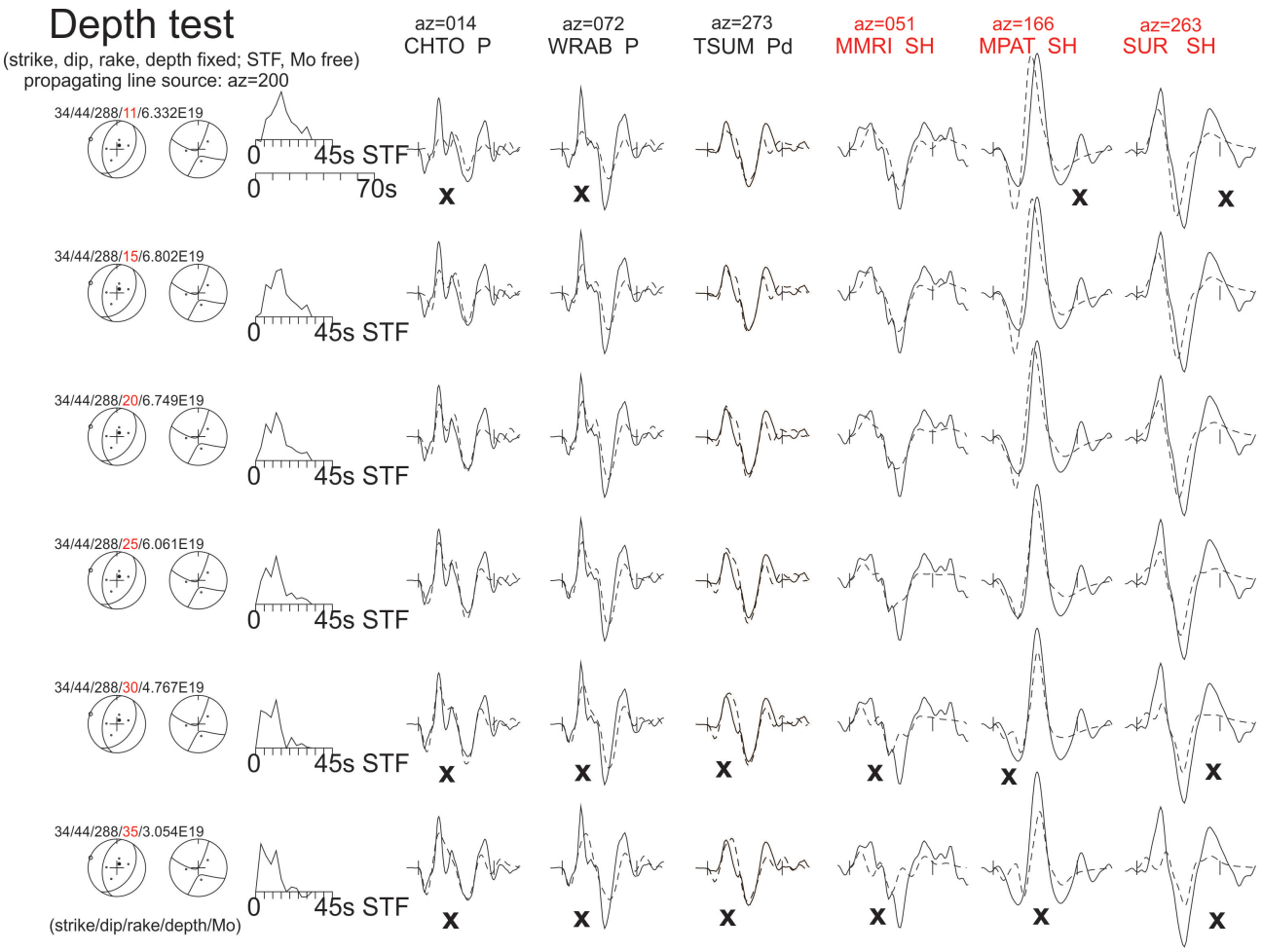

Figure 7: Tests to show the sensitivity to depth of the SSW-propagating line source, and the trade-offs between source time function (STF), depth and seismic moment. See text for details.

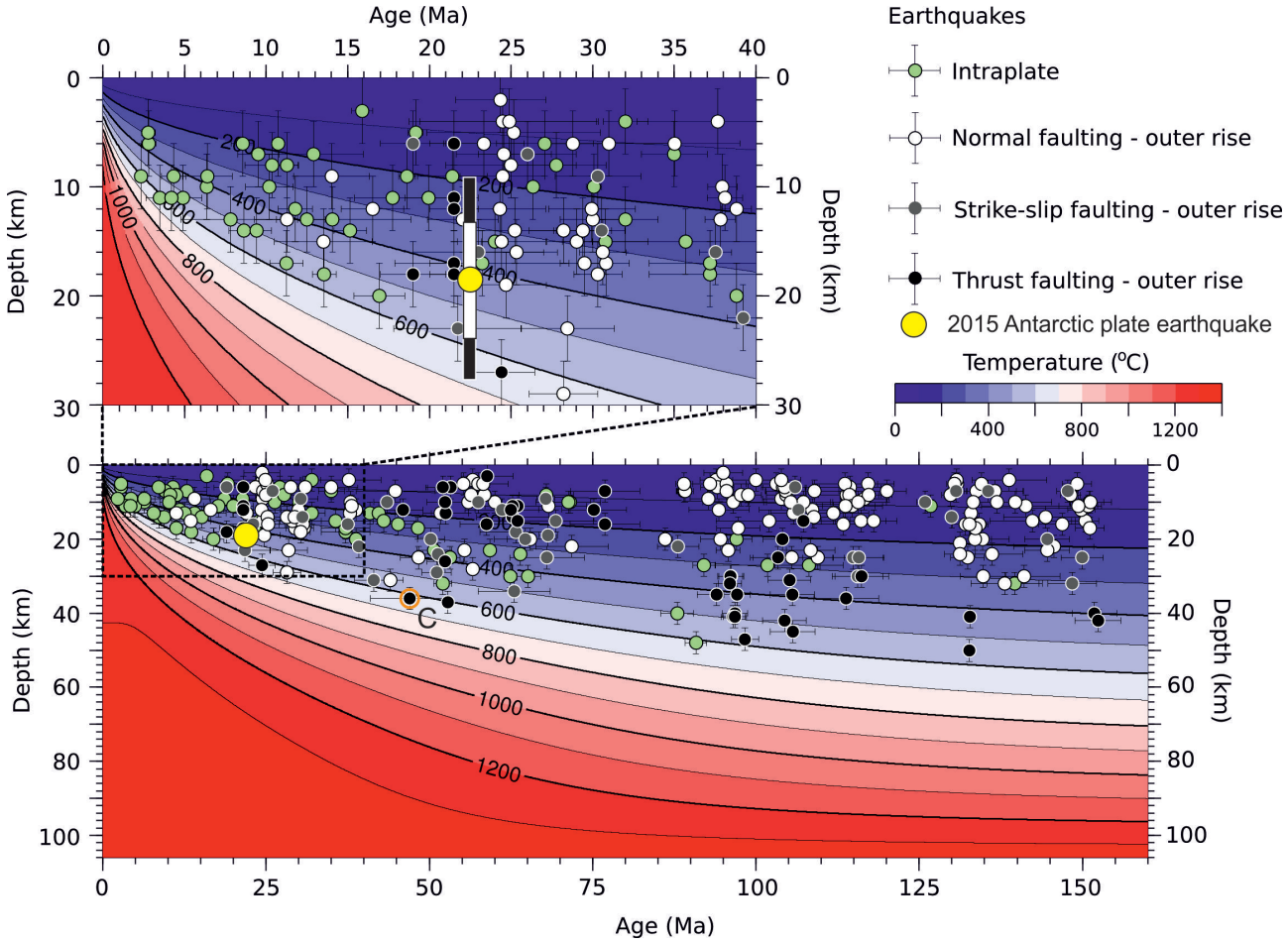

Figure 8: Depths of intraplate oceanic earthquakes as a function of lithosphere age and temperature, adapted from Craig *et al.* (2014). The top panel is a detail of age range 0–30 Ma. Our determination of the centroid of the 2015 Antarctic plate earthquake, for the SSW-propagating line source, is the yellow circle. The white bar shows the probable depth extent of faulting, with black error bars. The circled event marked C at 50 Ma is the centroid redetermination by Craig *et al.* (2014) of the 1964 Chile outer-rise earthquake, which had been similarly mis-assigned.